

Observational Properties of Nonthermal Emission from Relativistic Jets Escaping Active Galactic Nucleus Disks

KEN CHEN^{1,2} AND ZI-GAO DAI^{1,2}

¹*Department of Astronomy, School of Physical Sciences, University of Science and Technology of China, Hefei 230026, China; cken@ustc.edu.cn, daizg@ustc.edu.cn*

²*School of Astronomy and Space Science, University of Science and Technology of China, Hefei 230026, People's Republic of China*

ABSTRACT

Relativistic jets launched from stellar-mass compact objects embedded in the accretion disk of an active galactic nucleus (AGN) can produce nonthermal emission upon successfully breaking out of the disk. In this paper, we present a comprehensive study of the long-term propagation dynamics and broadband nonthermal radiation signatures of such jets in a realistic AGN environment, explicitly modeled as wind outflows. Our modeling reveals two distinct features imprinted by the high-density AGN medium: rapid deceleration of the jet ejecta, accompanied by a prompt downshift of the emission spectral energy distribution, and persistently strong synchrotron self-absorption, giving rise to a prominent quasi-thermal hump in the emission spectrum. Crucially, both gamma-ray burst jets and jets powered by accreting binary black hole merger remnants can produce detectable multi-wavelength emissions that substantially outshine the AGN background. Moreover, the short time delays between gravitational wave triggers and these electromagnetic counterparts—typically less than 10^6 s—greatly facilitate secure multi-messenger associations. Besides, our findings highlight that interaction-induced radiation from AGN-embedded jet systems offers a powerful diagnostic probe of the spatial distribution, density structure, and physical properties of the AGN medium.

Keywords: Active galactic nuclei (16); Relativistic jets (1390); Gravitational wave sources (677); non-thermal radiation sources (1119);

1. INTRODUCTION

Relativistic jets with diverse powers and durations can be launched from a variety of extreme astrophysical events occurring in the accretion disk of an active galactic nucleus (AGN) (Chen & Dai 2025). In the era of multi-messenger astronomy, two representative classes of such disk-embedded jets have drawn particular attention: those associated with gamma-ray burst (GRB) and those driven by binary black hole (BBH) mergers.

GRBs originate either from the core collapse of massive stars (Woosley 1993; Woosley & Bloom 2006a) or from mergers of binary neutron star (BNS) and neutron star-black hole (NSBH) systems (Abbott et al. 2017a,b). Stars embedded in AGN disks can attain high masses and rapid rotation via efficient accretion (e.g., Dittmann et al. 2021; Jermyn et al. 2021; Fabj et al. 2025), rendering them promising progenitors for long GRBs (Woosley & Heger 2006b). AGN disks are also considered fertile environments for BNS and NSBH mergers (McKernan et al. 2020; Yang et al. 2020; Perna et al. 2021a). Motivated by these prospects, extensive efforts have been

devoted to modeling GRB jets within AGN disks, encompassing jet propagation (Zhu et al. 2021; Zhang et al. 2024), the production and diffusion of prompt emission and afterglow radiation (Perna et al. 2021b; Lazzati et al. 2022; Wang et al. 2022; Ray et al. 2023; Kang et al. 2025; Zhao 2026), as well as the roles of jet structure (Kathirgammaraju et al. 2024; Yuan & Lei 2025), time-dependent energy injection (Huang et al. 2024), and prolonged central-engine activity (Wei et al. 2025). Nevertheless, all existing studies confine their environmental modeling exclusively to the AGN disk. Even when jet dynamics and afterglow evolution after disk breakout are considered, the overlying ambient medium is routinely approximated as a uniform interstellar medium (ISM), which is a substantial oversimplification.

AGN disks are also compelling sites for BBH mergers (e.g., Tagawa et al. 2020; Ishibashi & Gröbner 2024; McKernan et al. 2025; Rowan et al. 2025; Delfavero et al. 2025; Ford & McKernan 2025; Zhu et al. 2026), potentially accounting for anomalous gravitational-wave(GW) events such as GW190521 (Ab-

bott et al. 2020; Graham et al. 2020) and GW23123 (Abac et al. 2025; He et al. 2025; Bartos & Haiman 2026). Moreover, the gas-rich environment of an AGN disk enables the post-merger remnant to launch a relativistic jet through accretion (e.g., McPike et al. 2026). Thermal emission produced during jet breakout from the disk and the subsequent expansion of the cocoon formed by jet-AGN disk interaction have been investigated by several studies (Tagawa et al. 2023, 2024, 2026; Chen & Dai 2024, 2025; Rodríguez-Ramírez et al. 2024). To date, however, only Wang et al. (2021) has explored the dynamical evolution and consequent radiation following the jet ejecta emergence from the disk.

AGN disks are geometrically thin, occupying only a small fraction of the overall AGN space. Thus, once a jet successfully breaks out of the disk, its subsequent interaction with the overlying AGN environment gives rise to nonthermal emission that persists far longer than its thermal counterpart, rendering it a crucial observational probe of such systems. Moreover, the AGN environment above the disk is far from an ISM-like state, and is instead characterized by high-density gas—manifesting as clumpy clouds or large-scale outflows—and an intense radiation field (Netzer 2013). Despite its importance, the long-term propagation of jets in this environment and the resulting broadband nonthermal radiation remain largely unexplored.

In this paper, we investigate the observational signatures of nonthermal emission generated by a relativistic jet that successfully escapes the AGN disk and subsequently propagates through the overlying AGN medium. A schematic diagram is depicted in Figure 1. We model the co-evolution of propagation dynamics and multi-wavelength emission for jets with varying power and duration, explicitly accounting for their interaction with the high-density AGN gas. We further assess their detectability and calculate the resulting multiband light curves. As a complementary study to Chen & Dai (2025), this work completes the radiation characteristics of the AGN-disk jet beyond the thermal breakout phase. The paper is organized as follows. In Section 2, we describe our modeling of the AGN gas distribution, the jet dynamics, and the emission processes. Section 3 presents a comprehensive analysis of the non-thermal emission for three representative jet systems—a powerful uncollimated jet, a long-lived free jet, and an under-accelerated jet at breakout—focusing specifically on GRB jets and BBH merger remnant-driven jets. In Section 4, we discuss the detectability and multi-band light curves of these jets. We summarize our main results and provide discussion in Section 5. Symbols G

and c in this paper represent the gravitational constant and the speed of light, respectively.

2. JET PROPAGATION IN AGN ENVIRONMENT

2.1. AGN gas distribution

To investigate the long-term propagation of a jet initially embedded in an AGN accretion disk throughout the broader AGN environment, the gas distribution in both the AGN disk and the circum-disk medium is required. For the AGN disk, following our previous work (Chen & Dai 2025), we adopt the radial structure model of Sirko & Goodman (2003), where at each disk radius R_0 , the density $\rho_d(R_0)$ and scale height $H_d(R_0)$ of the disk are explicitly specified. The disk is approximated as a thin slab vertically bounded by H_d , with a uniform vertical gas number density profile given by

$$n = \rho_d(R_0)/m_p, \quad r < H_d \quad (1)$$

where r is the vertical distance from the disk midplane, and m_p is the proton mass.

Above the disk, the observed broadening of emission lines indicates the presence of a large number of dense clouds, spanning density from $10^{8-10} \text{ cm}^{-3}$ in the broad-line region to 10^{3-5} cm^{-3} in the narrow-line region, confined by a relatively low-density hot intercloud medium (Netzer 2013). Besides the clouds, multiple classes of outflows are detected in most AGNs from the observation of blue-shifted absorption lines (Laha et al. 2021), confirming the prevalence of an outflow in an AGN¹. Accretion disk winds provide a physically motivated origin for AGN outflows, with launch and acceleration processes feasible in AGN scenarios (e.g., Proga et al. 2000; Risaliti & Elvis 2010; Giustini & Proga 2019). Moreover, these winds would naturally give rise to the clouds via condensation processes (Netzer 2013). In practice, the launch and acceleration mechanisms differ among distinct classes of AGN outflows (Laha et al. 2021); aiming to characterize the key features of jet-AGN medium interaction, the wind structure is simplified into a uniform global form (King & Pounds 2015)

$$\dot{M}_w \simeq 4\pi b n_w R^2 m_p v_w, \quad (2)$$

filling the AGN environment, where \dot{M}_w is the wind mass-loss rate, b is the covering factor, n_w is the gas number density at a radial distance R from the central

¹ The non-detection of these absorption lines would reflect a sporadic nature of the outflow, which exhibits a low gas column density feature during observation, rendering the line becoming too weak to detect (King & Pounds 2015).

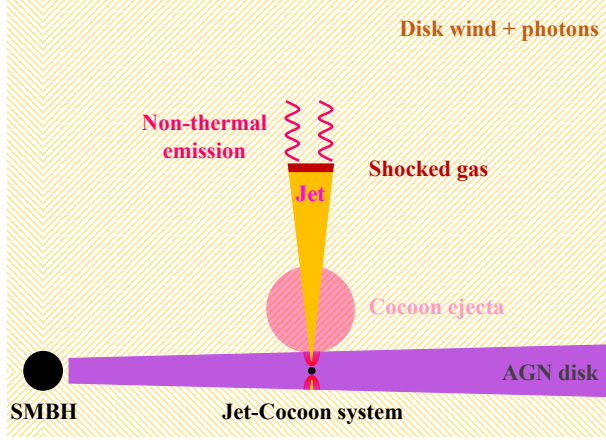


Figure 1. Schematic description of a jet successfully breaking out of the AGN disk and propagating through the AGN environment. AGN-driven wind outflows and AGN photons fill the region above the disk. The interaction between the jet and the ambient medium drives strong shock, producing nonthermal emission via particle acceleration. Besides, the cocoon, formed by the energy deposition from the jet propagating within the disk, expands under its own pressure.

super-massive black hole (SMBH), one has

$$n_w = 6.2 \times 10^7 \text{ cm}^{-3} \left(\frac{b}{0.5} \right)^{-1} \left(\frac{\dot{M}_w}{0.1 \dot{M}_{\text{Edd}}} \right) \left(\frac{R}{10^3 R_g} \right)^{-2} \left(\frac{v_w}{10^9 \text{ cm s}^{-1}} \right)^{-1}, \quad (3)$$

for a SMBH of mass $M = 10^7 M_\odot$, which is consistent in magnitude with the observation (Laha et al. 2021). The corresponding vertical gas density profile above the AGN disk is modeled as (e.g., Zhou et al. 2023)²

$$n = n_0 \left(\frac{\sqrt{R_0^2 + r^2}}{\sqrt{R_0^2 + H_d^2}} \right)^{-2} \simeq n_0 \left[1 + \left(\frac{r}{R_0} \right)^2 \right]^{-1}, \quad r > H_d \quad (4)$$

where R_0 is the radius of the AGN disk where the jet launches, $n_0 = n_w(\sqrt{R_0^2 + H_d^2}) \sim 10^8 \text{ cm}^{-3}$ for $M = 10^7 M_\odot$ and $R_0 = 10^3 R_g$. When the jet propagation distance is much smaller than R_0 , the ambient density remains approximately constant, i.e., $n \sim n_0$; at a large distance, the density approaches a wind-like profile, i.e., $n \propto r^{-2}$. In this work, we neglect the ambient cloud medium. Jet-cloud interactions are expected to produce

additional emission signals (e.g., Zhuang et al. 2025), which will be studied in a future work.

2.2. Jet dynamics

When a jet propagates through an extremely dense environment, such as AGN disk, the interaction between its head and the surrounding medium continuously shocks gas, which then flows laterally to inflate a cocoon with large pressure, encasing and collimating the jet body (e.g., Begelman & Cioffi 1989; Matzner 2003; Bromberg et al. 2011). The dynamics of jet propagation within the AGN disk have been investigated in detail in Chen & Dai (2025). As the jet head is significantly decelerated, for a jet with duration $t_{j,\text{cri}}$, the jet tail catches up to the head precisely at the time, t_{bre} , the head breaking out of the disk surface, resulting in the disappearance of jet body. Jets with duration $t_{j,0} < t_{j,\text{cri}}$ therefore become choked, where $t_{j,\text{cri}}$ denotes the critical jet duration, whose value is shown in Figure 5 of Chen & Dai (2025). In this paper, we focus on jets that successfully escape the AGN disk, i.e., those with $t_{j,0} > t_{j,\text{cri}}$, and for simplicity, assume the jet launches at the disk midplane, propagating vertically (perpendicular to the disk plane).

For a successful jet, its power L_j and duration $t_{j,0}$ jointly determine the initial properties when propagating in the AGN environment, specifically, the effective duration and the Lorentz factor (LF). On the one hand, as the leading segment of the jet with duration $t_{j,\text{cri}}$ transforms into the cocoon material, the remaining jet has a reduced duration $t_j = t_{j,0} - t_{j,\text{cri}}$. On the other hand, the overpressured cocoon compresses the jet body, driving a collimating shock inside the jet, of which the

² Note that n exhibits a sharp discontinuity at the disk surface H_d . In reality, the density profile transitions continuously—from the AGN accretion disk, through the local disk wind, to the global AGN wind. Fortunately, the disk density declines rapidly above H_d , following either a Gaussian distribution $n \propto \exp[-r^2/(2H_d^2)]$ or a polytropic profile $n \propto (1-r^2/(6H_d^2))^3$ (e.g., Kato et al. 2008); within a few H_d , n decreases from ρ_d/m_p to n_0 . This decline slightly modifies the initial properties of the successful jet (Chen & Dai 2025), such as reducing its duration after the breakout. Moreover, the jet deceleration radius where the reverse shock becomes relativistic is significantly larger than H_d , as confirmed by Equation (12). Consequently, the detailed vertical structure of the AGN disk has only a minor influence on the jet long-term nonthermal emission.

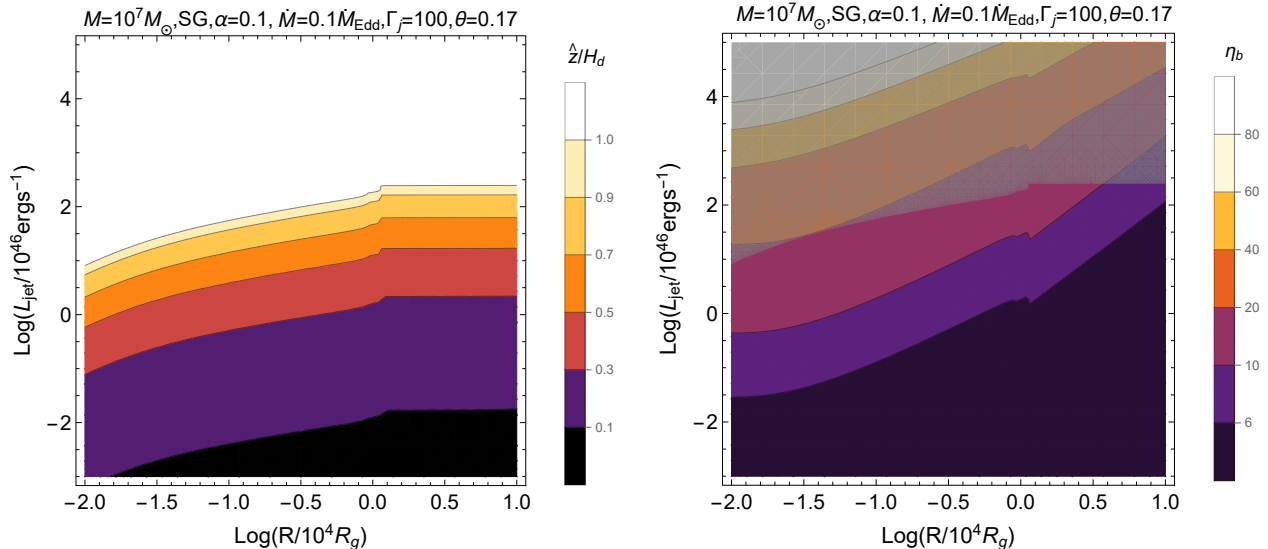


Figure 2. Properties of the shocked materials in the successful jets at breakout. The left panel shows the distance from the jet base to the collimating shock converge point, within which the jet remains predominantly unshocked, and beyond it the jet material is shocked to resist the cocoon pressure. The right panel shows the critical baryonic loading of the shocked jet material, which determines the terminal LF the materials can be accelerated after breaking out of the AGN disk. The grey region indicates parameter space where the entire jet remains uncollimated and unshocked within the disk.

convergence height is (Bromberg et al. 2011)

$$\hat{z} \simeq \left(\frac{L_j}{\pi c P_c} \right)^{\frac{1}{2}}, \quad (5)$$

assuming that the jet acceleration radius is much smaller than \hat{z} , where the cocoon pressure P_c is calculated following Chen & Dai (2025). Below \hat{z} , the jet propagates freely with an initial LF $\Gamma_j = \Gamma_0$; above \hat{z} , the jet material passes through the collimating shock, where it is shocked, thermalized, and decelerated to a LF $\Gamma_j = 1/\theta_0$, with most of its kinetic energy converted into internal energy, where θ_0 is the initial opening angle of the jet (Bromberg et al. 2011).

As shown in Figure 2, when breaking out of the AGN disk at t_{bre} , a powerful jet remains uncollimated and largely unshocked, provided that $\hat{z} > H_d$ and the collimating shock has not yet converged. Conversely, if the collimating shock converges below the disk surface, the jet segment between \hat{z} and H_d is shocked prior to breakout. Consequently, the LF of the jet at the onset of propagation in the AGN environment falls into three regimes. In the first regime, the remnant jet remains unshocked, with $\Gamma_j = \Gamma_0$, which requires $\hat{z} > H_d$. In the second regime, the jet duration satisfies $t_{j,\text{cri}} < t_{j,0} \lesssim t_{\text{bre}}$, so the earliest-emerging jet segment is shocked and thermalized. Subsequently, it undergoes self-acceleration and reaches a terminal LF of $\Gamma_j = \max[\Gamma_0, \eta_b]$, where η_b denotes the critical baryonic loading, determining the maximum LF attainable before photon-baryon decouples and photon-acceleration halts, which is given by

(Nakar et al. 2005; Nakar & Piran 2017)

$$\eta_b = \left(\frac{L_j \sigma_T}{2\pi \theta_0^2 R_j m_p c^2} \right)^{\frac{1}{4}}, \quad (6)$$

where σ_T is the Thomson scattering cross-section, and R_j is the lateral radius of the jet at its breakout. As shown in Figure 2, the shocked jet material is inefficiently accelerated, forming a shell with a LF $\eta_b < \Gamma_0$. Subsequently, the trailing unshocked jet component catches up and collides with this slower shell, launching an internal shock that drives reacceleration. In the early phase following jet breakout, the expanding cocoon maintains sufficient pressure to continuously compress jet segments embedded within the AGN disk, thereby producing additional shocked jet material, which persists for approximately a cocoon dynamical timescale $t_{\text{coc}} = R_c/v_c$ (Mizuta & Ioka 2013). Calculating the jet-cocoon evolution within the AGN disk following Chen & Dai (2025), we find that $t_{\text{coc}} \sim t_{\text{bre}}$. The third regime corresponds to a long-lived jet, defined by $t_{j,0} \gg t_{\text{bre}}$, in which the cocoon thermal pressure declines continuously and dramatically during its expansion, rendering it incapable of compressing the jet. As a result, the bulk of jet material remains unshocked, and the jet retains its initial LF $\Gamma_j = \Gamma_0$.

After the jet is injected into the AGN environment above the AGN disk and interacts with the swept ambient gas, a forward shock (FS) is driven into the AGN medium, while a reverse shock (RS) simultaneously

propagates back through the jet. Applying shock jump conditions and adopting the uniform pressure and LF assumption across the shocked AGN medium (region 2) and the shocked jet (region 3), the LF of the post-shock fluid can be calculated as (Sari & Piran 1995; Metzger et al. 2012)

$$\gamma_2 = \gamma_3 = \Gamma_j \left[1 + 2\Gamma_j \left(\frac{n}{n_j} \right)^{\frac{1}{2}} \right]^{-\frac{1}{2}}, \quad (7)$$

where

$$n_j = \frac{L_j}{\pi\theta^2 r^2 m_p c^3 \Gamma_j^2} \quad (8)$$

is the jet density at the radius r , and θ is the jet opening angle. The number density, internal energy density and total number of protons in region 2 evolve as

$$n_2 \simeq 4\gamma_2 n, \quad (9)$$

$$e_2 = 4(\gamma_2 - 1)\gamma_2 n m_p c^2, \quad (10)$$

$$N_2 = \int_{H_d}^r \pi\theta^2 r^2 n dr. \quad (11)$$

As the jet propagates through the dense AGN medium, the criterion for a RS to become relativistic, i.e. (Zhang 2018)

$$\Gamma_j^2 \frac{n_j}{n} = 137 \left(\frac{L_j}{10^{50} \text{ erg s}^{-1}} \right)^{-1} \left(\frac{\Gamma_j}{100} \right)^4 \left(\frac{\theta}{0.1} \right)^2 \left(\frac{n}{10^8 \text{ cm}^{-3}} \right) \left(\frac{r}{10^{15} \text{ cm}} \right)^2 \gg 1, \quad (12)$$

is typically satisfied. Therefore, the parameters of relativistic RS evolve as

$$n_3 \simeq 4\gamma_{43} n_j, \quad (13)$$

$$e_3 = 4(\gamma_{43} - 1)\gamma_{43} n_j m_p c^2, \quad (14)$$

$$N_3 = \frac{L_j}{\Gamma_j m_p c^2} \frac{r}{2\gamma_3^2 c}, \quad (15)$$

where the relative LF between the jet shock upstream and downstream is

$$\gamma_{43} \simeq \frac{1}{2} \left(\frac{\Gamma_j}{\gamma_3} + \frac{\gamma_3}{\Gamma_j} \right). \quad (16)$$

The radius at which the RS crosses the entire jet is

$$r_c = \left(\frac{L_j t_j^2}{\pi\theta^2 n m_p c} \right)^{\frac{1}{4}}, \quad (17)$$

and the corresponding observed crossing time is $t_{\text{cross}} = r_c/2\gamma_3^2 c$. In this paper, an on-axis observer is considered, and viewing angle effects are not taken into account.

After the RS fully crosses the jet, the evolution of its downstream parameters is approximately described by (e.g., Yi et al. 2013)

$$\begin{aligned} \gamma_3 &= \gamma_{3,c} (r/r_c)^{\frac{(2k-7)}{2}}, \quad n_3 = n_{3,c} (r/r_c)^{\frac{(2k-13)}{2}}, \\ e_3 &= e_{3,c} (r/r_c)^{\frac{(4k-26)}{3}}, \quad N_3 = N_{3,c}, \end{aligned} \quad (18)$$

where the subscript ‘‘c’’ denotes values evaluated at r_c , and k is an index of the environmental density decay, which is simply set to 0 for $r < R_0$ and 2 for $r > R_0$ based on the density distribution of Equation (4). $\gamma_3 = 1$ is adopted as the termination condition for the RS evolution, since the relativistic self-similar solution described by Equation (18) becomes invalid once the RS transitions into the Newtonian regime. Although this threshold is artificial, it slightly influences the observed nonthermal emission signature, because late-time emission is dominated by the FS.

For the FS, the fluid dynamics is governed by the following coupled differential equations (Huang et al. 2000)

$$\frac{dr}{dt} = \beta c \Gamma \left(\Gamma + \sqrt{\Gamma^2 - 1} \right), \quad (19)$$

$$\frac{dm}{dr} = 2\pi r^2 (1 - \cos\theta) n m_p, \quad (20)$$

$$\frac{d\Gamma}{dm} = -\frac{\Gamma^2 - 1}{M_j + \epsilon m + 2(1 - \epsilon)\Gamma m}, \quad (21)$$

$$\frac{d\theta}{dt} = \frac{c_s (\Gamma + \sqrt{\Gamma^2 - 1})}{r}, \quad (22)$$

where Γ , m , θ are the LF, mass, opening angle of the swept-up and shocked AGN medium, $M_j = L_j t_j / \Gamma_j c^2$ is the total jet mass, ϵ is the radiative efficiency of the fluid, i.e., the fraction of internal energy lost via radiation per dynamical timescale, and the sound speed is

$$c_s^2 = \hat{\gamma}(\hat{\gamma} - 1)(\Gamma - 1) \frac{1}{1 + \hat{\gamma}(\Gamma - 1)} c^2, \quad (23)$$

with the adiabatic index $\hat{\gamma} \sim (4\Gamma + 1)/3\Gamma$.

2.3. Emission equations

Within the collisionless shocks generated by the jet-AGN gas interaction, electrons are compressed and accelerated to relativistic energy (e.g., Sironi et al. 2013), of which the distribution can be described by a power law (Huang & Cheng 2003; Wang et al. 2026)

$$\frac{dN_e}{d\gamma} \propto (\gamma - 1)^{-p}, \quad \gamma_m \leq \gamma \leq \gamma_M, \quad (24)$$

where γ_m and γ_M are the minimum and maximum LF of the accelerated electrons, respectively. The index p

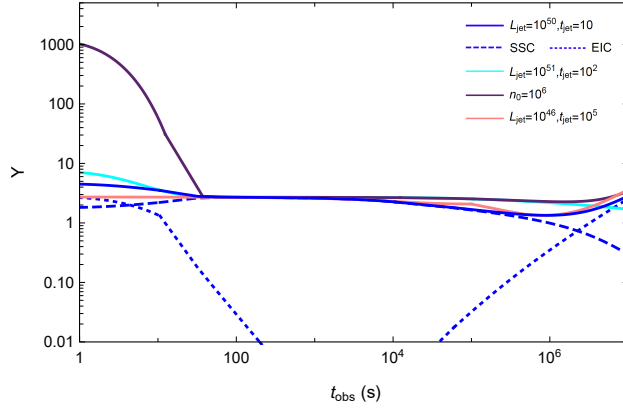


Figure 3. Comparison of the synchrotron, synchrotron self-Compton scattering, and external inverse-Compton scattering emission luminosity. Solid lines show the total Compton–synchrotron Y_{TOT} , with each line corresponding to various parameters in the power and duration of the jet system, as well as the ambient density. All jets are set to launch at $R_0 = 10^3 R_g$ of an accretion disk surrounding a SMBH of mass $M = 10^7 M_\odot$, and $n_0 = 10^8 \text{ cm}^{-3}$. Dashed and dotted lines denote the SSC–synchrotron Y_{SSC} and EIC–synchrotron Y_{EIC} , respectively, for the $L_j = 10^{50} \text{ erg s}^{-1}$ and $t_j = 10 \text{ s}$ case.

depends on the detailed microscopical processes and the magnetization of both the jet and the ambient material, and evolves as the shock transitions from the ultra-relativistic to the non-relativistic regime (Zhang 2018). GRB observations indicate that p is event-dependent, ranging from values below 2 to above 3, with a typical value of 2.2–2.3 consistent with theoretical expectations (Wang et al. 2015). We adopt a fiducial value $p = 2.3$ to describe the electron energy distribution, while we note that p may deviate from this value and evolve during jet propagation. Assuming a fraction ξ_e of electrons are accelerated, consuming a fraction ϵ_e of the shock internal energy, the average LF of these electrons is given by

$$(\bar{\gamma} - 1)\xi_e n_e m_e c^2 = \epsilon_e (\Gamma - 1) n_p m_p, \quad (25)$$

where n_e and n_p are the number density of electrons and protons in the shocked fluid, and Γ is the LF of the post-shock gas. For a pairless hydrogen shock, one has $n_p/n_e = 1$. For the distribution of Equation (24), the average LF can be expressed as $\bar{\gamma} - 1 \simeq \frac{p-1}{p-2}(\gamma_m - 1)$ for $\gamma_m \ll \gamma_M$ and $p > 2$, and thereby the minimum LF of electrons is

$$\gamma_m = \frac{p-2}{p-1} \frac{\epsilon_e}{\xi_e} \frac{m_p}{m_e} (\Gamma - 1) + 1, \quad (26)$$

which can be extended to the Newtonian regime, where $\Gamma - 1 \sim \frac{1}{2}\beta_{\text{sh}}^2$, and

$$\beta_{\text{sh}} = \left[2 \frac{p-1}{p-2} (\gamma_m - 1) \frac{\xi_e}{\epsilon_e} \frac{m_e}{m_p} \right]^{\frac{1}{2}}. \quad (27)$$

Since only relativistic electrons effectively produce non-thermal radiation, we adopt a critical LF $\gamma_{m,\text{cri}} = 2$, below which the electron contribution to the emission becomes negligible (Granot et al. 2006; Sironi et al. 2013).

For $p = 2.3$ and $\xi_e = 1$, the corresponding critical shock velocity is $\beta_{\text{cri}} = 0.22(\epsilon_e/0.1)^{-0.5}$. When $\beta_{\text{sh}} > \beta_{\text{cri}}$, it can be considered that essentially all electrons are accelerated to be relativistic; conversely, when the shock decelerates into the deep Newtonian regime (Huang & Cheng 2003), as occurs during jet propagating within the AGN environment, only a fraction $\xi_e < 1$ of electrons attains relativistic energies. As shown in Equation (27), assuming ϵ_e remains approximately constant across the shock evolution, one has $\xi_e \propto \beta_{\text{sh}}^2$, the resulting relativistic electron fraction is given by

$$\xi_e = \min\left[1, \left(\frac{\beta_{\text{sh}}}{\beta_{\text{cri}}}\right)^2\right], \quad (28)$$

and the minimum LF of the accelerated electron is adjusted to $\min[\gamma_m, 2]$.

Besides accelerating electrons, shocks also amplify magnetic fields. Assuming a fraction ϵ_B of the shock internal energy is converted into magnetic fields, the comoving-frame magnetic energy density is given by

$$U_B = \frac{B'^2}{8\pi} = 4\epsilon_B (\Gamma - 1) \frac{\hat{\gamma}\Gamma + 1}{\hat{\gamma} - 1} n m_p c^2, \quad (29)$$

where the prime denotes the quantity measured in the the fluid comoving frame. For the RS, retaining the expressions for the internal energy and electron number density of the shocked fluid, γ_m and B' can be calculated as

$$\gamma_{m,R} = \frac{p-2}{p-1} \epsilon_e \frac{e_3}{n_3 m_e c^2} + 1, \quad (30)$$

and

$$B'_R = (8\pi\epsilon_B e_3)^{\frac{1}{2}}. \quad (31)$$

For simplicity, we adopt uniform values $\epsilon_e = 0.1$ and $\epsilon_B = 0.01$ across both the FS and RS regions, al-

though the actual values of these microphysical parameters are event-dependent, ranging over $\epsilon_e \in (10^{-2}, 0.5)$ and $\epsilon_B \in (10^{-6}, 0.5)$ (e.g., [Santana et al. 2014](#)), and may vary significantly between FS and RS ([Zhang 2018](#)).

AGN environments consist of both gas and photons originating from the AGN disk and corona. During the interaction between the jet and this multi-component medium, relativistic electrons in the shocked fluid simultaneously produce synchrotron radiation and inverse Compton scattering, where both the synchrotron photons and the AGN photons are upscattered. Thus, the nonthermal emission arises from three distinct radiative processes: synchrotron emission, synchrotron self-Compton (SSC) scattering, and external inverse Compton (EIC) scattering, the total luminosity of which is

$$L_{\text{nonthermal}} = L_{\text{syn}} (1 + Y_{\text{TOT}}), \quad (32)$$

where $Y_{\text{TOT}} = Y_{\text{SSC}} + Y_{\text{EIC}}$ is the total Compton enhancement factor, with $Y_{\text{SSC}} = L_{\text{SSC}}/L_{\text{syn}}$ and $Y_{\text{EIC}} = L_{\text{EIC}}/L_{\text{syn}}$ are the SSC and EIC luminosity ratios relative to the synchrotron luminosity, respectively. Derived from the same population of electrons, the single-electron power ratio provides a robust proxy for the relative intensity of these three emissions, i.e., $Y_{\text{SSC}} \simeq U_{\text{syn}}/U_B = \beta_{\text{sh}} U_e/U_B (1 + Y_{\text{TOT}})$ ([Sari & Esin 2001](#)), and $Y_{\text{EIC}} \simeq U_{\text{AGN}}/U_B$, where U_{syn} , U_e and U_{AGN} are the fluid comoving-frame energy densities of the synchrotron radiation field, the relativistic electrons, and the external AGN radiation field, respectively ([Zhang 2018](#)).

Treating the AGN disk radiation as the external photon field, its comoving-frame energy density at a specific distance $R = \sqrt{R_0^2 + r^2}$ from the central SMBH under the unidirectional light assumption can be calculated as

$$U_{\text{AGN}} \simeq \Gamma^4 (1 - \beta \cos i)^4 \cos i \frac{\eta \dot{M} c}{4\pi R^2}, \quad (33)$$

where \dot{M} and η are the accretion rate and radiative efficiency of the AGN disk, the first two terms correspond to the Doppler factor, i is the angle between the disk normal and the direction of photon propagation from the inner disk toward the shock, with $\cos i = r/R$, and the third term accounts for the effective radiative area of the disk. Substituting Y_{EIC} , one has

$$Y_{\text{SSC}} = \frac{-(1 + Y_{\text{EIC}}) + \sqrt{(1 + Y_{\text{EIC}})^2 + 4\beta_{\text{sh}}\epsilon_e/\epsilon_B}}{2}. \quad (34)$$

As shown in [Figure 3](#), for our fiducial ϵ_B , the EIC component dominates the electron cooling only during two evolutionary phases of jet propagation in the AGN environment: the early ultra-relativistic phase, where

strong Doppler boosting significantly enhances U_{AGN} , resulting in $U_{\text{AGN}} \gg U_B$ even when ϵ_B assumes an extreme value of 0.5; and the late Newtonian phase, where declining shock power reduces the magnetic energy density, thereby suppressing synchrotron and increasing Y_{EIC} . Since $Y_{\text{EIC}} \propto \epsilon_B^{-1}$, lowering ϵ_B further amplifies the contribution of EIC cooling. However, for most jet events, the EIC component remains subdominant during the trans-relativistic evolutionary phase, unless ϵ_B is significantly reduced below fiducial value. In that regime, EIC becomes the dominant cooling channel, as synchrotron losses are suppressed due to the low magnetic field strength. Given that AGN are extended sources, calculating the EIC radiation requires spatially resolved background emission spectra. For $\epsilon_B = 0.01$, the EIC component remains subdominant across most jet evolutionary stages, we therefore adopt a simplified treatment by not modeling the EIC emission in detail, just incorporating its radiative contribution exclusively through Y_{TOT} , and we leave specific calculations in future work. Meanwhile, substantial variations in either ϵ_e or ϵ_B strongly affect the electron cooling feature when SSC dominates EIC $Y_{\text{SSC}} \gg Y_{\text{EIC}}$, in which case $Y_{\text{TOT}} \sim Y_{\text{SSC}} \sim \sqrt{\beta_{\text{sh}}\epsilon_e/\epsilon_B}$.

The comoving-frame peak specific synchrotron emission power of a single electron is ([Rybicki & Lightman 1979](#))

$$P_{\nu, \text{max}} = \frac{\sqrt{3} B' e^3}{m_e c^2}, \quad (35)$$

and its total emission power is

$$P_{\text{syn}}(\gamma) = \frac{4}{3} \sigma_T c \gamma^2 \beta^2 U_B. \quad (36)$$

Including both SSC and EIC cooling contributions, the radiative energy rate for an electron with LF γ can be written as

$$\frac{d\gamma}{dt} m_e c^2 = -P_{\text{syn}} (1 + Y_{\text{TOT}}), \quad (37)$$

and the corresponding characteristic radiative cooling timescale is given by

$$t_c = \left| \frac{\gamma}{\dot{\gamma}} \right| = \frac{6\pi m_e c^2 \gamma}{\sigma_T c (\gamma^2 - 1) B'^2 (1 + Y_{\text{TOT}})}. \quad (38)$$

Equating this cooling time with the electron acceleration timescale $t_{\text{acc}} \simeq \gamma m_e c / e B'$, the maximum LF attainable by relativistic electrons is

$$\gamma_M = \left[\frac{6\pi e}{\sigma_T B' (1 + Y_{\text{TOT}})} \right]^{\frac{1}{2}}, \quad (39)$$

which is much larger than other characteristic LFs. Meantime, the cooling LF, γ_c , is defined by equating

t_c with the fluid comoving dynamical timescale t' , i.e. (Wang et al. 2026)

$$\gamma_c = \frac{1}{2} \left(\bar{\gamma}_c + \sqrt{\bar{\gamma}_c^2 + 4} \right), \quad (40)$$

where

$$\bar{\gamma}_c = \frac{6\pi m_e c}{\sigma_T B'^2 (1 + Y_{\text{TOT}}) t'}. \quad (41)$$

For an on-axis observer, one has $t' \simeq 2\Gamma t_{\text{obs}}$, where t_{obs} denotes the observed time measured from the moment of successful jet breakout.

Before escaping the emission region, synchrotron photons would experience a frequency-dependent self-absorption by the radiating electrons, which modifies both the electron energy distribution and the observed radiation spectrum. Below the characteristic absorption frequency ν'_a , synchrotron emission is optically thick, and thus, photons are self-absorbed and radiation is suppressed, displaying a thermal-like spectral distribution in Rayleigh-Jeans regime (Sari & Piran 1999). Consequently, ν'_a can be estimated via equating the synchrotron flux with the blackbody flux (e.g., Shen & Zhang 2009; Wang et al. 2026), i.e.

$$I_{\nu}^{\text{syn}}(\nu'_a) = I_{\nu}^{\text{bb}}(\nu'_a) = 2kT \frac{\nu_a'^2}{c^2}, \quad (42)$$

and

$$kT \sim \max[\gamma_a, \min(\gamma_c, \gamma_m)] m_e c^2, \quad (43)$$

where the LF of an electron and its characteristic synchrotron emission frequency is connected through $\nu' = 3eB'\gamma^2/4\pi m_e c$. In the strong self-absorption regime, where $\nu'_a > \nu'_c$, the self-absorbed photons would heat the electrons and prevent their cooling down to γ_c they would otherwise attain. This process transforms both the electron energy distribution and the photon spectrum into a quasi-thermal form below γ_a on a timescale shorter than t' (Ghisellini et al. 1988), giving rise to a thermal bump in electron energy distribution and a corresponding thermal hump in emission spectrum (Kobayashi et al. 2004). The detailed expressions of ν'_a are presented in Appendix A. The broadband synchrotron spectrum $F_{\nu}(\nu)$ and the electron energy distribution $N_e(\gamma)$ are fully determined by the relative ordering of the three key characteristic frequencies, which are presented in Appendix B. For an on-axis observer, the observed photon frequency is Doppler-boosted as $\nu \sim 2\Gamma\nu'$. Throughout the remainder of this paper, we adopt the observer-frame frequency.

Considering first-order inverse Compton scattering, given the electron energy distribution $N_e(\gamma)$ and the synchrotron photon spectrum $F_{\nu}(\nu_s)$, where ν_s is the frequency of these seed photons, the flux spectrum of

the SSC emission is given by (Sari & Esin 2001; Gao et al. 2013a)

$$\begin{aligned} F_{\nu, \text{SSC}}(\nu) &= \Delta \sigma_T \int_2^{\infty} d\gamma \frac{dN_e}{d\gamma} \int_0^{x_0} dx F_{\nu}(x) \\ &= \sigma_T \int_2^{\infty} d\gamma \frac{d\Sigma_e}{d\gamma} \int_0^{x_0} dx F_{\nu}(x), \end{aligned} \quad (44)$$

where Δ is the thickness of the emission region, Σ is the column density of the electrons, $x = \nu/4\gamma^2\nu_s$ and $x_0 = 0.5$. In the strong absorption regime, inverse Compton scattering involving seed photons with $\nu_s < \nu_a$ and electrons with LF $\gamma < \gamma_a$ is suppressed, as both components are thermalized and no longer participate in nonthermal scattering processes.

3. NONTHERMAL EMISSION PROPERTIES

By combining the dynamical and radiative equations presented in Sections 2.2 and 2.3, we model the co-evolution of jet propagation dynamics and nonthermal radiation in an AGN ambient medium. For simplicity, we adopt $\epsilon \sim \epsilon_e$, and examine three representative jet systems that escape the AGN disk, which collectively span the key parameter space governing jet-medium interaction—namely, a powerful uncollimated jet, a long-lived free jet, and an under-accelerated jet at breakout—to elucidate their distinct dynamical and radiative properties.

3.1. Powerful uncollimated jet

A fully uncollimated jet at breakout from the AGN disk requires a power $L_j \gtrsim 10^{48}$ erg s⁻¹, as shown in Figure 2. GRB jets with $L_j \gtrsim 10^{50}$ erg s⁻¹ provide a compelling astrophysical realization of such disk-embedded relativistic jets. As shown in Figure 6 of Chen & Dai (2025), at the inner region of the AGN disk within $R_0 \lesssim O(10^3)R_g$, long GRB jets with $t_{j,0} \sim 10 - 100$ s can successfully break out of the disk. Though short GRB jets with $t_{j,0} < 2$ s require breakout from a more inner disk region—typically associated with lower-mass SMBHs where the AGN disk scale height is reduced, a plausible hyper-Eddington accretion process would open a low-density circum-binary cavity penetrating through the disk prior to binary merger (Chen et al. 2023), thereby preventing jet choking and enabling its sustained relativistic propagation (Zhang et al. 2024; Yuan & Lei 2025). Here, we construct a representative short-duration uncollimated jet event to investigate its dynamical and radiative properties: a relativistic jet with power $L_j = 10^{50}$ erg s⁻¹ launches at $R_0 = 10^3 R_g$ of an

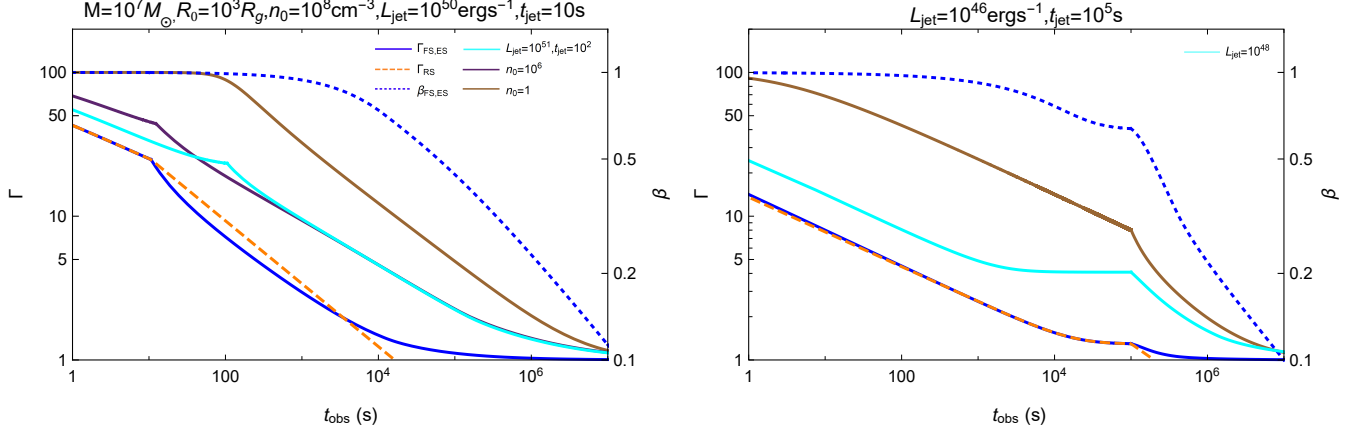


Figure 4. Dynamics of jets propagating within the AGN environment. The left panel shows the dynamical evolution of a jet with $L_j = 10^{50} \text{ erg s}^{-1}$ and $t_j = 10 \text{ s}$, where the blue line, orange dashed line, and blue dotted line represents the LF of forward shock, LF of reverse shock, and the velocity of forward shock, respectively. The cyan and purple line exhibits the LF of forward shock, changing the system parameter to a more powerful and long-lived jet with $L_j = 10^{51} \text{ erg s}^{-1}$ and $t_j = 100 \text{ s}$, and a lower-density ambient medium $n_0 = 10^6 \text{ cm}^{-3}$, respectively. For comparison with the canonical environment, the interstellar medium case is also presented, where $n_0 = 1 \text{ cm}^{-3}$. The right panel shows a long-lived jet case with $L_j = 10^{46} \text{ erg s}^{-1}$ and $t_j = 10^5 \text{ s}$, where the cyan line changes the jet power to $L_j = 10^{48} \text{ erg s}^{-1}$.

AGN disk surrounding a SMBH of mass $M = 10^7 M_\odot$ ³, successfully escapes the disk and injects into the AGN ambient medium, with an initial LF $\Gamma_j = 100$ and a reduced duration $t_j = 10 \text{ s}$.

While the density of the AGN wind medium is lower than that of the underlying AGN disk, it remains substantially higher than the density of typical interstellar or intergalactic environments. Consequently, the relativistic jet experiences strong and rapid ram-pressure deceleration during propagation. As shown in the left panel of Figure 4, the bulk LF of the shock has begun to decline significantly during the early phase of coupled forward–reverse shock evolution. Following RS crossing at $t_{\text{cross}} \sim t_j$, deprived of further jet energy injection, the FS undergoes markedly accelerated deceleration relative to the pre-crossing phase. As a result, the external shock evolves to a non-relativistic velocity on a timescale of $O(10^4) \text{ s}$. In contrast, when the same jet propagates through a uniform ISM with number density $n_0 = 1 \text{ cm}^{-3}$, the forward shock maintains a significantly higher bulk Lorentz factor and remains relativistic at the same t_{obs} . Increasing the jet power and duration—e.g., to $L_j = 10^{51} \text{ erg s}^{-1}$ and $t_j = 100 \text{ s}$ —or decreasing the AGN ambient density—e.g., to $n_0 = 10^6 \text{ cm}^{-3}$ —mitigates FS deceleration: in the former case, ram-pressure driving is stronger and more

sustained; in the latter, ambient inertia provides weaker braking.

In the strong shock driven by jet-AGN medium interaction, the evolution of nonthermal radiation exhibits distinguishing features, as shown in Figure 5. First, synchrotron emission remains persistently in the strong self-absorbed regime where $\gamma_a > \gamma_c$, owing to the extremely high ambient number density⁴. At early times, $\gamma_c \sim 1$ with $\bar{\gamma}_c \ll 1$, indicating that radiative cooling is extremely efficient, such that only a small fraction of the relativistic electron population contributes to the instantaneous emission (Rahaman et al. 2025). Second, given that $\gamma_m - 1 \propto \Gamma - 1$, the rapid deceleration of the FS drives a corresponding decline in γ_m . When $t_{\text{obs}} > 10^3 \text{ s}$, γ_m drops below γ_a , shifting the dominant emission mechanism to synchrotron self-absorption thermalization. At late times, the Newtonian shock accelerates electrons inefficiently, resulting in $\gamma_m = 2$ and a substantial reduction in the fraction of radiating relativistic electrons. Third, the short propagation distance over which deceleration occurs yields a high density of the shocked jet material, which consequently raises $\gamma_a > \gamma_m > \gamma_c$ in the RS.

The evolution of the three characteristic synchrotron frequencies— ν_m , ν_a , and ν_c —which jointly govern the shape of the broken power-law spectrum, is shown in Figure 5. Also displayed is the critical frequency of the SSC emission, defined as $\nu_{\text{SSC}} =$

³ In the AGN merger channel, a substantial fraction of binary compact object (e.g., BBH) mergers are expected to occur within the AGN disks surrounding SMBHs of mass $M = O(10^7) M_\odot$ (Rowan et al. 2025).

⁴ Self-absorption is more extreme in the AGN disk environment (Wang et al. 2022).

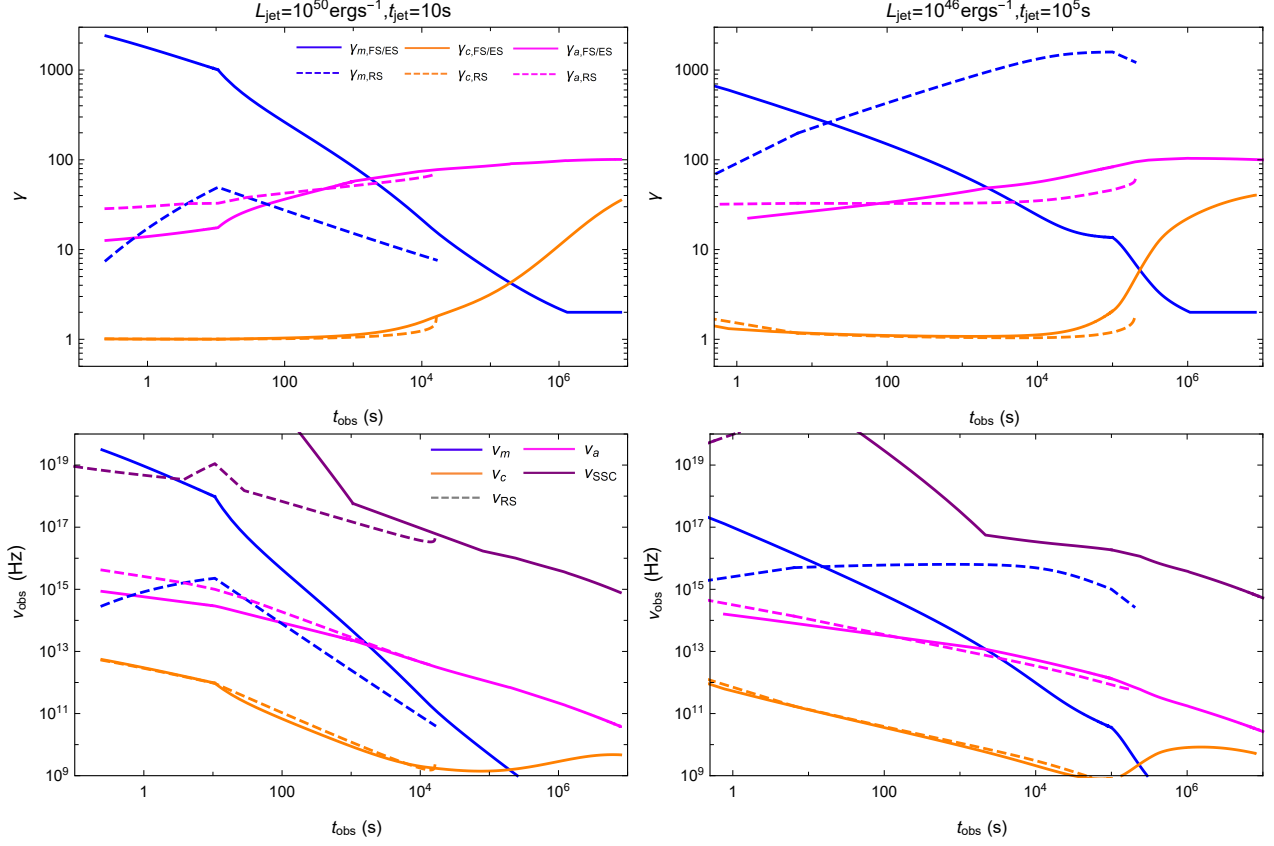


Figure 5. Characteristic Lorentz factors and emission frequencies of relativistic electrons. In each panel, the solid and dashed lines represent the parameters in FS and RS. The blue, orange, and magenta line denotes the minimum LF γ_m , the cooling LF γ_c , and the synchrotron self-absorption LF γ_a , respectively. In addition to the associated synchrotron frequencies, the critical frequencies for SSC scattering are shown in the $t_{\text{obs}}-\nu_{\text{obs}}$ panels. The RS-related parameter evolution is artificially truncated at $\gamma_3 = 1$. The left panels show a $L_j = 10^{50} \text{ erg s}^{-1}$ and $t_j = 10 \text{ s}$ system, while the right panels show a $L_j = 10^{46} \text{ erg s}^{-1}$ and $t_j = 10^5 \text{ s}$ system.

$4x_0 \max[\gamma_a, \gamma_m, \gamma_c]^2 \max[\nu_a, \nu_m, \nu_c]$ (Sari & Esin 2001; Gao et al. 2013a). All these frequencies decrease with time, systematically shifting the spectral energy distribution (SED) toward lower energies. The SED exhibits distinct features across epochs, as shown in Figure 6. Overall, as $\gamma_a > \gamma_c$, self-absorption process heats the cooling electrons up and produces a thermal hump around ν_a (Kobayashi et al. 2004). At early time $t_{\text{obs}} = 10 \text{ s}$, the FS SED displays two spectral breaks at ν_a and ν_m , peaking at ν_m . In contrast, RS generates a more luminous SED, peaking at ν_a . SSC emission from the RS peaks at a lower frequency than that from the FS, yielding low-frequency RS-SSC flux comparable to the FS synchrotron component. During the intermediate time $t_{\text{obs}} = 10^3 \text{ s}$ and 10^5 s , the ν_m break gradually approaches ν_a and ultimately vanishes. Concurrently, the FS synchrotron luminosity declines continuously, accompanied by a downward shift of the peak frequency ν_a . As both ν_a and the corresponding LF γ_a decrease, the FS SSC spectrum softens and its luminosity diminishes.

At this epoch, synchrotron and SSC emission from the RS are both subdominant relative to their FS counterparts. At late time $t_{\text{obs}} = 10^7 \text{ s}$, the radiation evolution follows the same trend: the total flux continues to fade, and the spectral peak shifts progressively toward lower frequencies.

As the jet resides in AGN, its emitted radiation must be assessed relative to the background emission (gray-dotted line in Figure 6). In our fiducial case, the jet emission exceeds the AGN background across multiple wavelength bands at early phases; at late times, although it drops below the background at high frequencies, the jet remains the dominant contributor to the transient radio-IR emission from its host AGN. Increasing the jet power and duration can produce a longer-lasting, multiband-observable emission (second panel in Figure 6), its SED evolution closely resembles that of the fiducial case. A low-density AGN environment markedly alters the jet emission properties (third panel in Figure 6). At early times, e.g., $t_{\text{obs}} = 10 \text{ s}$, the lower magnetic

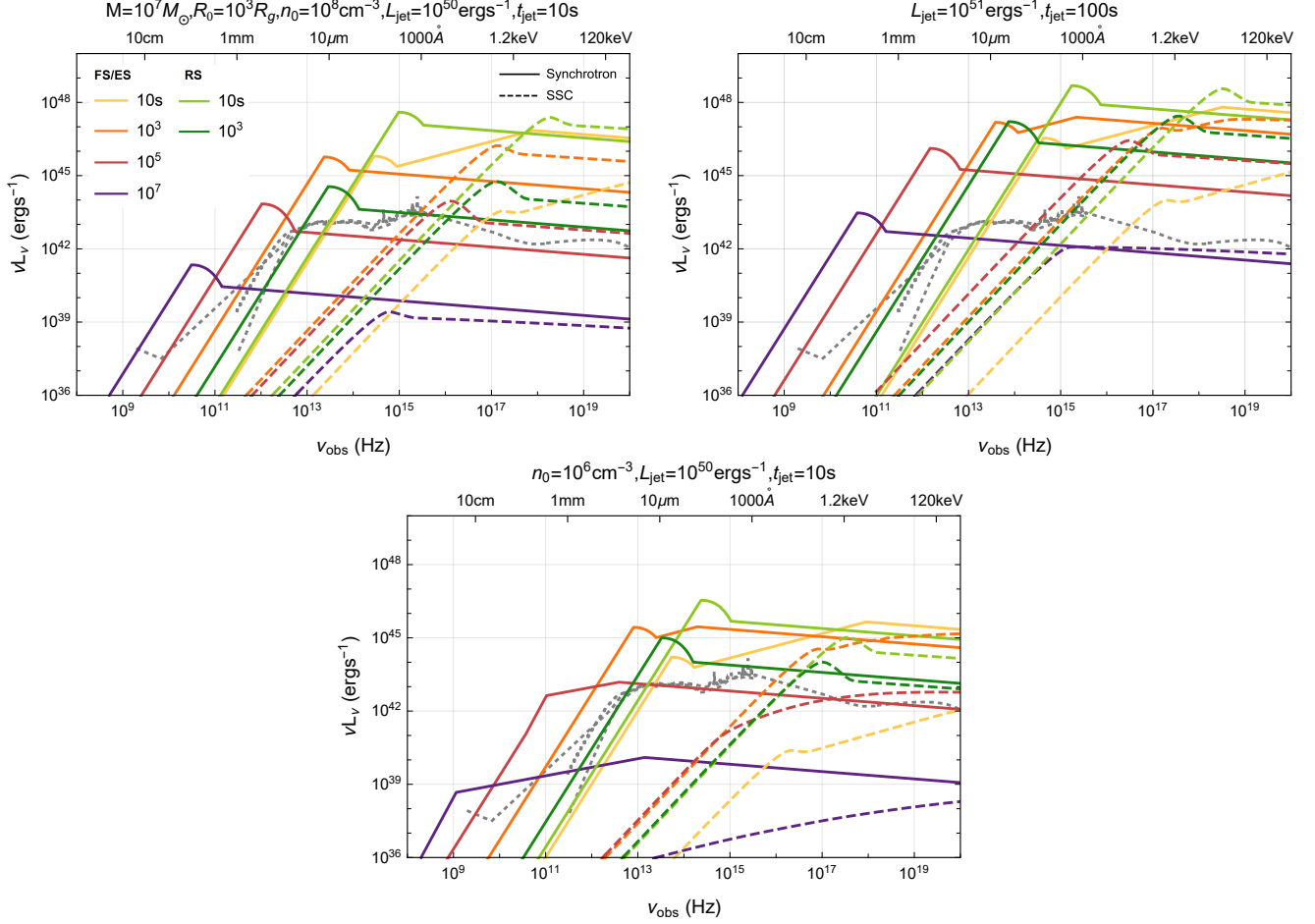


Figure 6. Spectral energy distributions of nonthermal emissions for GRB jet cases. Each panel corresponds to different parameter: $L_j = 10^{50} \text{ erg s}^{-1}$ and $t_j = 10 \text{ s}$, $L_j = 10^{51} \text{ erg s}^{-1}$ and $t_j = 100 \text{ s}$, and $n_0 = 10^6 \text{ cm}^{-3}$. Emissions from both the forward and reverse shock at various observer times are presented, where solid lines denote synchrotron radiation, while the dashed lines denote SSC emission. As a benchmark for comparison, the mean spectral energy distribution of radio-quiet quasars from Shang et al. (2011) is shown as the grey dotted line. The far-infrared band constitutes a key radiation channel for jet systems; however, the composite SED from Shang et al. (2011) lacks far-infrared data. Two infrared-specific spectral SED with the different extent of subtraction for the galaxy contribution are adopted, where the middle dotted line corresponds to the SED from Symeonidis et al. (2016), and the bottom dotted line corresponds to the SED from Lyu & Rieke (2017).

energy density downstream of the FS and the higher bulk LF of the shock jointly yield a large Y_{EIC} . Consequently, EIC process strongly suppresses both synchrotron and SSC emissions, leading to significantly reduced broadband luminosity. At late times, ν_a decreases significantly in a tenuous medium, shifting the broken power-law spectrum to follow $\nu_m < \nu_a < \nu_c$ regime, markedly distinct from that observed in high-density environments. Therefore, nonthermal emission from the jet system serves as a powerful probe of the gas profile in the AGN environment.

3.2. Long-lived free jet

The duration of a long-lived free jet satisfies $t_{j,0} \gg t_{\text{bre}}$. Jets launched by BBH mergers embedded in

AGN disk fulfil this condition and therefore constitute a representative example of this jet class. Due to the anisotropy of gravitational-wave emission, the remnant black hole acquires a recoil velocity and subsequently moves through the AGN disk, where it accretes ambient magnetized gas and launches a jet (Chen & Dai 2024). The jet luminosity can be estimated as (Kaaz et al. 2023; Kim & Most 2025)

$$\begin{aligned}
 L_j &= \eta \dot{M}_{\text{BHL}} c^2 \\
 &= 1.3 \times 10^{46} \text{ erg s}^{-1} \left(\frac{\eta}{0.05} \right) \left(\frac{\dot{M}_{\text{BHL}}}{2.3 \times 10^{26} \text{ g cm}^{-3}} \right),
 \end{aligned} \tag{45}$$

where η denotes the effective energy conversion efficiency, \dot{M}_{BHL} is evaluated for an accretion system that

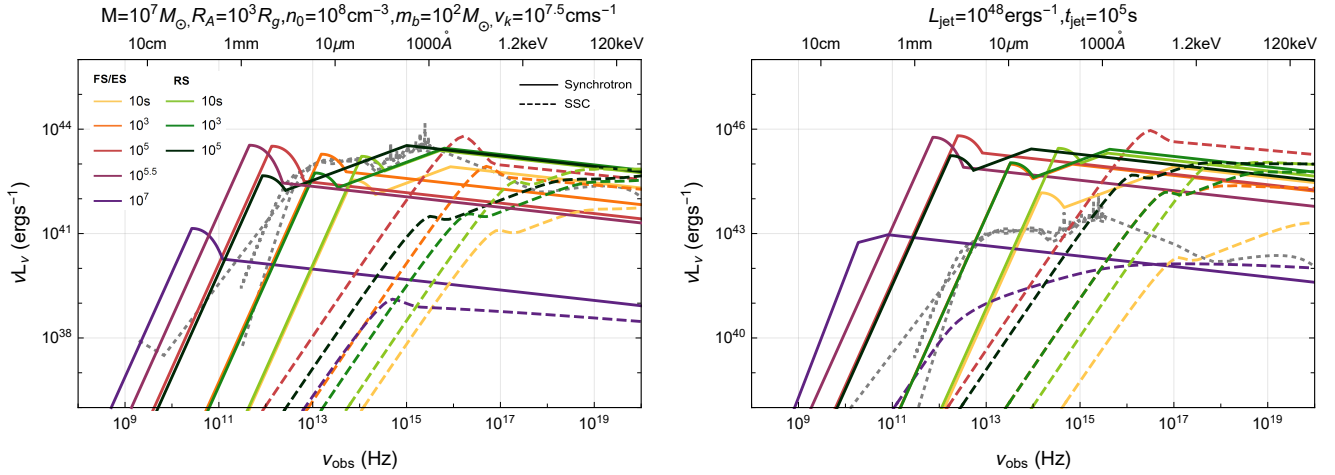


Figure 7. Spectral energy distributions of nonthermal emissions for BBH remnant-driven jet cases. The left panel depicts a relativistic jet with $L_j = 10^{46} \text{ erg s}^{-1}$ and $t_j = 10^5 \text{ s}$, consistent with the jet launched in a BBH merger system of mass $m = 100M_\odot$, where the remnant BH receives a kick velocity of $v_k = 10^{7.5} \text{ cm s}^{-1}$. The right panel corresponds to a more powerful jet with $L_j = 10^{48} \text{ erg s}^{-1}$.

a BH of mass $m = 100M_\odot$ moves at $v_k = 10^{7.5} \text{ cm s}^{-1}$ through the AGN disk at $R_0 = 10^3 R_g$ around a SMBH of mass $M = 10^7 M_\odot$ (Chen & Dai 2024). The jet duration is highly sensitive to the magnetic properties of the AGN disk. Driven by the magnetorotational instability, the disk magnetic field is turbulent, with field directions randomized but exhibiting approximate coherence over H_d scale (e.g., Salvesen et al. 2016). For a given magnetic field inclination angle related to the BH spin, the duration of an individual jet corresponds to the accretion timescale t_{BHL} (Kim & Most 2025). Besides, the jet is quenched once the ambient magnetic field reorients or the remnant BH escapes the AGN disk; both processes occur on a characteristic timescale $t_k \sim H_d/v_k$. Consequently, the jet duration is $t_{j,0} = \min[t_{\text{BHL}}, t_k]$. As shown in Figure 2 of Chen & Dai (2024), for launching radii $R_0 \gtrsim$ a few hundred R_g , we have $t_{\text{BHL}} < t_k$. Thus, we conservatively adopt

$$t_{j,0} \simeq t_{\text{BHL}} = \frac{Gm}{v_k^3} = 4.1 \times 10^5 \text{ s} \left(\frac{m}{100M_\odot} \right) \left(\frac{v_k}{10^{7.5} \text{ cm s}^{-1}} \right)^{-3} \quad (46)$$

As shown in Figure 4 of Chen & Dai (2025), the jet breakout time is typically less than one day. Therefore, a kicked remnant—acting as the central engine—remains active over an extended period during its driven jet propagating through the AGN environment, continuously injecting unshocked material to push the FS and RS. Here, we investigate this representative jet, adopting $L_j = 10^{46} \text{ erg s}^{-1}$, $t_j = 10^5 \text{ s}$, and $\Gamma_j = 100$.

The FS-RS evolution phase persists for $t_{\text{cross}} \sim t_j$. When propagating through a low-density ISM, the FS can maintain relativistic velocity over long timescales, as shown in the right panel of Figure 4. In contrast,

within the AGN environment, owing to high ambient gas density and moderate jet power, the LF of the shocked fluid decreases significantly over time: it falls to ~ 10 at early time $t_{\text{obs}} = 1 \text{ s}$, and even becomes non-relativistic despite continued energy injection from the ongoing jet. Once all the jet materials are shocked, the FS undergoes an extreme braking, as evidenced by a sharp decline in velocity β . Another distinctive feature is that the LF of the shocked fluid asymptotically flattens once the FS-RS system propagates over sufficiently large distances, where the AGN environment exhibits wind density profile. This behavior is prominent in jet system with $L_j = 10^{48} \text{ erg s}^{-1}$, arising from the identical radial dependence— $n(n_j) \propto r^{-2}$ —of the AGN and jet density, leading to an approximately constant LF, as demonstrated by Equation (7). The strong shock efficiently converts most of the jet kinetic energy into the internal energy of the shocked fluid, which subsequently powers substantial nonthermal emission.

As shown in Figure 5, the overall evolution of the characteristic LFs and frequencies of synchrotron emission closely mirrors that of the powerful uncollimated jet system analyzed in the previous section. Moreover, for the FS, its LF γ_m displays a flattened temporal evolution during the late FS-RS stage, attributable to the near-constant shock velocity sustained in the AGN wind medium. For the RS, γ_m is larger than the self-absorption LF γ_a , on account of its LF γ_{34} attaining a high value, which then produces a large post-shock electron energy density e_3 .

For the long-lived jet case, the most prominent feature is the prolonged persistence of the RS. As during the FS-RS evolution stage, the peak synchrotron flux of

RS fluid exceeds that of FS (Kobayashi & Zhang 2003); consequently, the radiation is dominated by the RS over a broad spectral range, shown in Figure 7. The SED at various epochs generally exhibits a thermal hump at ν_a , arising from the strong self-absorption. For the $L_j = 10^{46}$ erg s $^{-1}$ jet, the emission remains comparable to or exceeds the background at high frequencies during the FS-RS evolution phase, which is predominantly powered by the RS, with luminosity in these bands remaining approximately constant, arising from a combination of three effects: only a fraction of electrons radiate instantaneously, progressive strengthening of the RS, and Doppler boosting. At later times, as ν_a evolves to lower frequencies, where the background radiation is comparatively weaker, the emission becomes detectable. Increasing the jet power, e.g., to $L_j = 10^{48}$ erg s $^{-1}$, elevates the overall luminosity of the jet SED, rendering it brighter than the background radiation across multiple bands over an extended duration. Moreover, during the FS-RS evolution phase, the more powerful jet sustains higher shock velocity, leading to a slower decay of the FS emission and a late modest re-brightening, attributable to the near-constant shock velocity combined with an expanding shock surface area. After the RS crossing, comparison of the SEDs at $t_{\text{obs}} = 10^5$ s, $10^{5.5}$ s, and 10^7 s for both cases reveals that, the emission undergoes a slightly re-brightening episode, driven by the enhanced deceleration of FS following the cessation of jet energy injection, which thereby facilitates a more efficient conversion of ejecta kinetic energy into radiation.

3.3. Under-accelerated jet at breakout

Unlike the two jet classes analyzed above, when the initial jet duration satisfies $t_{j,\text{cri}} < t_{j,0} \lesssim t_{\text{bre}}$, at breakout, the emerging jet is initially shocked and photon-dominated with most of its energy residing in the radiation field, which subsequently accelerates the jet material. As shown in Figure 2, for an initial jet LF of $\Gamma_0 = 100$, the critical baryonic loading satisfies $\eta_b < 20$, meaning that the re-accelerating jet fails to reach its initial LF, and photons escape before the acceleration completes, with $1 - \eta_b/\Gamma_0 > 0.8$ of the jet initial energy consumed in the form of radiation, producing a transient flare. The duration of this emission is comparable to that of the energy injection into the shocked jet, which can be estimated as (Nakar & Piran 2017)

$$t_{j,\text{sh}} \approx t_{j,0}, \quad (47)$$

and its isotropic equivalent luminosity is

$$L_{j,\text{sh}} \approx \frac{2L_j}{\theta_0^2}. \quad (48)$$

The radiation temperature can be taken as (Nakar & Sari 2012)

$$T_{j,\text{sh}} \sim 100 \text{ keV}, \quad (49)$$

regulated by the positron-electron pair production.

As only a fraction of the jet total energy is deposited as kinetic energy, both the initial power and LF of the emerging jet are reduced compared to those of a free jet propagating through the AGN environment. This partially accelerated jet can nonetheless produce non-thermal radiation via shock interaction process with the ambient AGN medium, consistent with the scenarios discussed in Section 3.1 and 3.2. However, the lower jet power results in weaker radiative luminosity. Meanwhile, the jet decelerates more rapidly, leading to a faster-evolving SED compared to a free jet of identical duration and full acceleration. Moreover, the lower LF implies a smaller Doppler factor, which further reduces the early observed luminosity. As a result, the post-flare emission from the partially accelerated jet is observationally fainter and thus less detectable than that from its fully accelerated counterpart.

4. DETECTABILITY

For an AGN, the successful detection of emission from a stellar-object-driven jet depends not only on progressive improvements of telescope sensitivity, but also critically on whether the source intrinsic luminosity exceeds that of the background radiation. To assess detectability, we investigate multi-wavelength light curves of the targeted jet systems, taking the corresponding AGN background radiation as the baseline.

4.1. Gamma-ray burst

As revealed by the SED as shown in Figure 6, the GRB jet emission outshines the background across multiple observational bands. Moreover, its total luminosity arises from the superposition of multiple radiation components—synchrotron emission and SSC scattering from both FS and RS—rendering complex structure in the light curves across different bands.

In the soft X-ray band (e.g., 1 keV), the dominant radiation mechanism responsible for the detected emission evolves across observational epochs, as shown in the upper left panel of Figure 8. During the early FS–RS evolution phase, synchrotron emission from the RS fluid dominates the observed flux. After RS crossing, its emission decays rapidly, and FS synchrotron component becomes dominant. Subsequently, as the critical frequency ν_{SSC} shifts through 1 keV, FS-SSC emission surpasses the fading synchrotron component, becoming the primary contributor to the soft X-ray flux. In contrast, RS-SSC emission remains the least luminous among the four

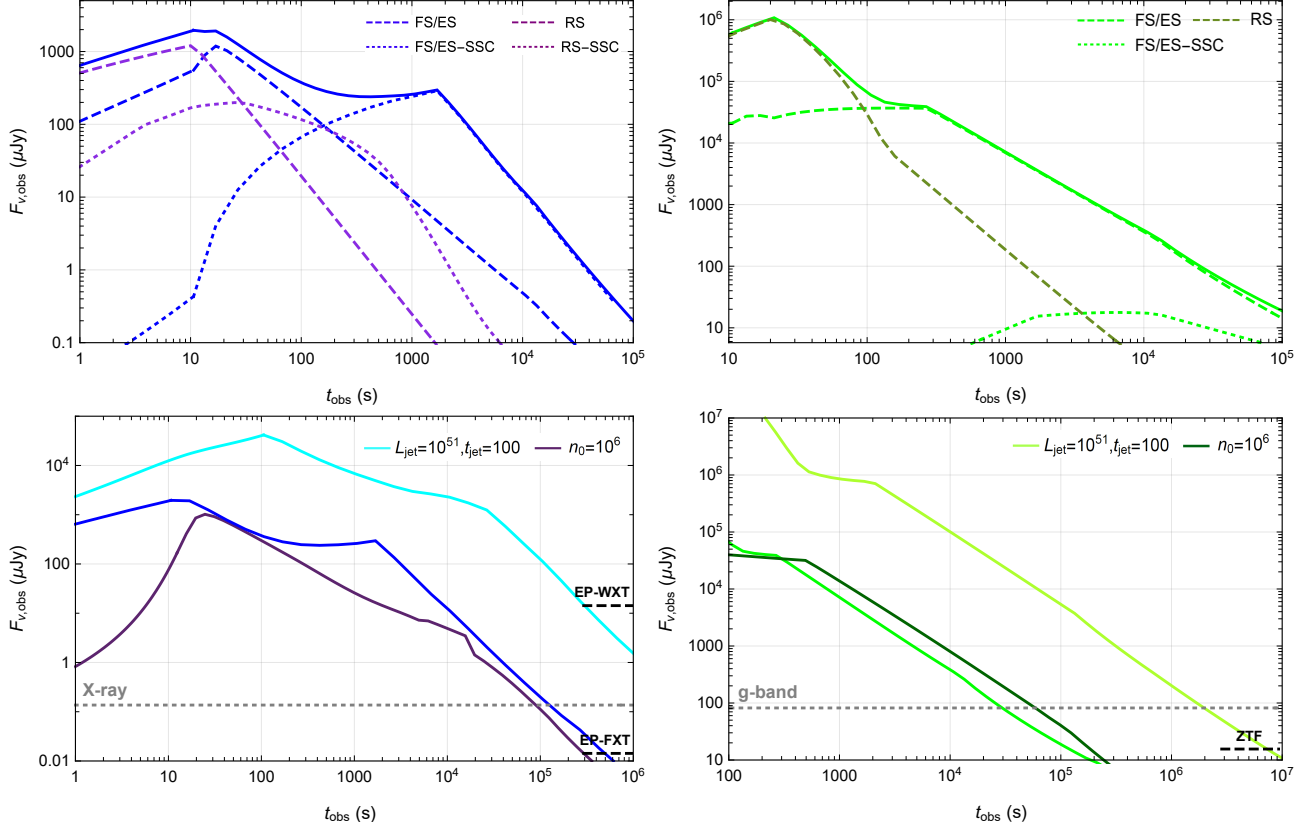


Figure 8. X-ray (left panels) and optical (g-band, right panels) light curves of GRB jet emission. The jet is set as $L_j = 10^{50}$ erg s $^{-1}$ and $t_j = 10$ s. The upper panels show the total observed flux evolution, decomposed into contributions from the FS and RS synchrotron components, and the corresponding SSC components. The lower panels display the light curves for varying parameters, where cyan and light green lines represent the $L_j = 10^{51}$ erg s $^{-1}$ and $t_j = 100$ s case, purple and dark green lines correspond to the $n_0 = 10^6$ cm $^{-3}$ case. The grey dashed lines indicate the flux level of AGN background in the respective band. Also shown are the detection sensitivities of the soft X-ray telescope Einstein Probe (EP) for 10 ks of exposure time (Yuan et al. 2022), and the optical telescope Zwicky Transient Facility (ZTF) for 30 s of exposure time (Bellm 2014).

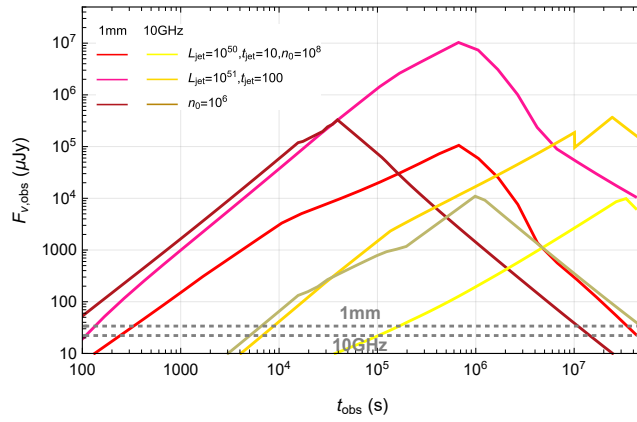


Figure 9. Same as Figure 8, but for infrared (1 mm) and radio (10 GHz) light curves of GRB jet emission.

components. Accordingly, in addition to the characteristic rise and decay phases, the light curve exhibits an approximately plateau-like structure during the transition from the synchrotron-dominated to the SSC-dominated regime (a similar feature is reported in Zhao (2026)). As shown in the lower left panel of Figure 8, the powerful GRB jet drives soft X-ray emission that rises significantly above the AGN background, yielding a detectable flare persisting for approximately one day. Increasing the jet power or duration enhances the peak luminosity of soft X-ray flare, and extends its observable time window to several days. Decreasing the ambient density significantly suppresses the early-time luminosity of both synchrotron and SSC emission. The AGN photons consume nearly all the energy of relativistic electrons via EIC scattering in both FS and RS, causing an early flux dip to emerge in the light curve⁵. Meanwhile, FS-SSC emission becomes dominant at a later epoch, preventing the emergence of a discernible plateau in the light curve.

As shown in the right panels of Figure 8, in the optical band (e.g., g-band), synchrotron emission from both the FS and RS jointly accounts for the gradual decay of the early-time light curve. Subsequently, the rapid fading of the RS component induces a steeper decay phase. Moreover, during the very early stage, strong self-absorption within the RS produces an optical thermal hump. SSC emission from both the FS and RS is too faint to yield a detectable contribution to the optical light curve. Given that this band is the dominant band of AGN background emission—due to its high intrinsic luminosity—the jet system can only produce flare with duration shorter than one day. A more powerful jet or a longer jet active time can concurrently enhance both the peak luminosity and duration of the optical flare.

In the infrared and radio band (e.g., 1 mm and 10 GHz), radiation is dominated almost exclusively by synchrotron emission from the FS. As the peak frequency of SED shifts into the infrared and radio bands during late-time epochs, the corresponding flares peak at $\sim 10^6$ s and $\sim 10^7$ s, respectively, as shown in Figure 9. The prominent decay structure observed in the light curves arises because ν_a and its driven thermal hump cross the observed frequency band, causing a plunge in emission luminosity. In a low-density environment (e.g., $n_0 = 10^6 \text{ cm}^{-3}$), the FS emission transitions from the strong-absorption regime to the weak-absorption regime, where $\nu_a < \nu_c$, at $\sim 10^4$ s. Subsequently, the thermal hump disappears, and the SED peak frequency downshifts into 1 mm and 10 GHz at an earlier time.

Concurrently, the peak flux densities in both bands are comparable to those in the high-density case. The flares produced by the jet system in these bands significantly outshine the AGN background, making them highly detectable transient signals. If the AGN disk-embedded BNS/NS-BH merger GW signal is detected, as the time delay of these EM transients is shorter than $O(10^6)$ s, the association between the GW-EM signals can be robustly confirmed. Moreover, this radiation component can induce transient modifications to the AGN SED on timescale of months to years—for instance, temporarily enhancing the radio-band luminosity sufficiently to reclassify a radio-quiet AGN as radio-loud.

Overall, GRB jets propagating through the AGN environment act as multi-wavelength emitters, producing detectable radiations across a broad spectral range, which exceed the sensitivity threshold of diverse telescopes.

4.2. BBH merger remnant-driven jet

For jets launched by the recoiling remnant of a BBH merger through accretion in the AGN disk (Chen & Dai 2024), exploring parameter spaces spanning kick velocity of $10^7 - 10^8 \text{ cm s}^{-1}$, AGN disk radius of $10^2 - 10^5 R_g$, and central SMBH mass of $10^6 - 10^9 M_\odot$, the jet power L_j reaches up to $O(10^{46}) \text{ erg s}^{-1}$ for $\eta = 0.05$, with the case presented in Section 3.2 serving as a representative example.

BBH merger remnant-driven jets are inefficient emitters of X-ray and optical radiation. As shown in Figure 10, for a $L_j = 10^{46} \text{ erg s}^{-1}$ jet, RS synchrotron emission produces a detectable soft X-ray flare lasting $\sim t_j$; however, the flare luminosity slightly exceeds the AGN background by only a small factor, limiting its significance. In the optical band, the jet emission—also dominated by RS synchrotron radiation—is comparable to the AGN background, rendering unambiguous identification challenging. In contrast, these jets produce prominent transient emissions in the infrared and radio bands. Whether by reducing the ambient density at $10^3 R_g$ to 10^6 cm^{-3} , setting the BBH merger at $10^4 R_g$, or increasing the SMBH mass to $10^8 M_\odot$, the jets can produce detectable infrared flares persisting for tens to hundreds of days. The same detectability is also achieved in the radio band, where these flares lag behind their infrared counterparts and persist for extended duration. However, radio flares are detectable only in AGN hosting low-mass SMBH, otherwise the background is intrinsically brighter, while the jet-induced flare emission in this environment is weaker. The light curve properties of these flares are generally consistent with those generated by GRB jets. Besides, the infrared flare

⁵ EIC scattering would produce intense soft X-ray emission.

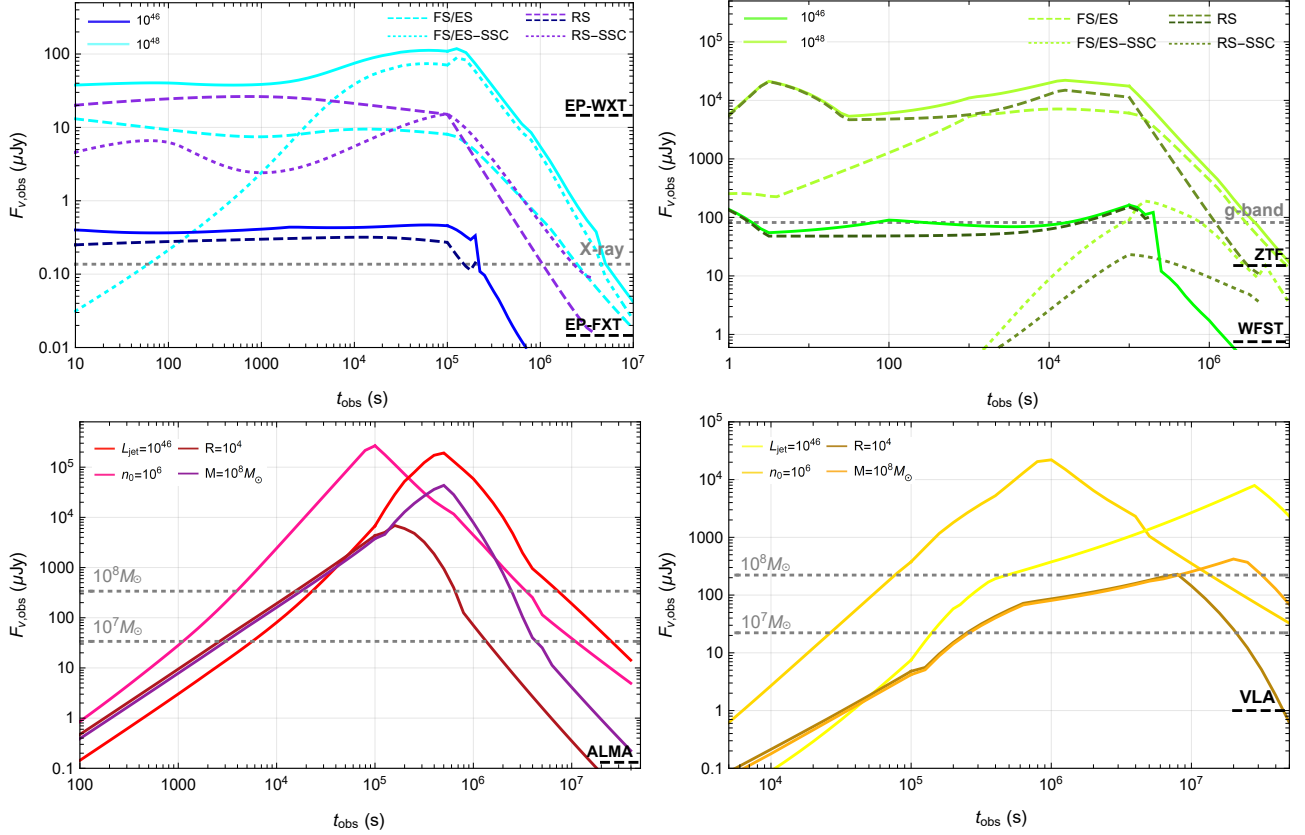


Figure 10. Multiband light curves of BBH merger remnant-driven jet emission. The jet is set as $L_j = 10^{46}$ erg s $^{-1}$ and $t_j = 10^5$ s. In the upper panels, the total emission and its radiative components from a more powerful jet with $L_j = 10^{48}$ erg s $^{-1}$ are also shown. The spikes and sharp declines observed in the light curves arise from the artificial termination of reverse shock evolution, along with its radiative contribution abruptly switched off. In the lower panels (1 mm for the left and 10 GHz for the right), three additional cases are presented, n_0 decreasing to 10^6 cm $^{-3}$, BBH merger occurring at $10^4 R_g$ of the AGN disk, and an increase in the SMBH mass to $10^8 M_\odot$, where the jet properties are recalculated via updated \dot{M}_{BHL} and t_{BHL} . The grey dashed lines indicate the flux level of AGN background with SMBH of $10^7 M_\odot$ and $10^8 M_\odot$. Also shown are the detection sensitivities of the optical telescope, Wide Field Survey Telescope (WFST), for 30 s of exposure time (Lei et al. 2023), the infrared telescope, Atacama Large Millimeter Array (ALMA), for 1 ks of exposure time, and the radio telescope, Very Large Array (VLA), for 1 ks of exposure time, calculated by their sensitivity calculators.

displays an additional distinctive feature: a steep rise at $t_{\text{obs}} \sim 10^5$ s, arising from the abrupt enhancement of FS deceleration following the end of FS-RS evolution. Most importantly, the time delay between jet launch and the onset of these detectable low-frequency transients is less than $O(10^5 - 10^6)$ s, facilitating their identification as EM counterparts to BBH merger GW events.

Increasing the jet power enables its X-ray and optical emission to sufficiently surpass the AGN background flux, e.g., to $L_j = 10^{48}$ erg s $^{-1}$, as shown in Figure 10. The long-lived RS synchrotron emission and the SSC scattering in FS successively dominate the X-ray flux, yielding an approximately flat and gradually rising light curve within $\sim t_j = 10^5$ s, followed by a decay. RS synchrotron emission also dominates the early optical flux, whereas FS synchrotron emission takes over in the

late phase, the resulting light curve exhibits a similar plateau to decline structure. In BBH merger remnant-driven jet scenario, although reducing the GW kick velocity could boost the jet power as $\dot{M}_{\text{BHL}} \propto v_k^{-3}$, the associated time delay between merger and jet launch, which $\sim t_{\text{BHL}} \propto v_k^{-3}$ (Kaaaz et al. 2023; Chen & Dai 2024), increases concomitantly. To launch a jet with $L_j = 3.3 \times 10^{46}$ erg s $^{-1}$, the remnant BH of mass $100 M_\odot$ moving through the AGN disk at $R_0 = 10^3 R_g$ from a SMBH of mass $M = 10^7 M_\odot$ requires a kick velocity as low as 10^7 cm s $^{-1}$, yielding $t_{\text{BHL}} = 4.4 \times 10^6$ s. Given such a prolonged time delay, the association between the observed EM flares and the GW event cannot be robustly established, which severely hampers observational follow-up. However, the recoil kick of the merger remnant can trigger a strong shock in the circum-

BBH accretion disk, enhancing gas angular momentum loss and thereby driving enhanced mass accretion (Rossi et al. 2010); under this mechanism, a higher efficiency $\eta = 1$ can substantially amplify the jet power to produce identifiable EM counterparts with short time delays (Tagawa et al. 2023).

In short, BBH merger remnant-driven jets are detectable in the infrared and radio bands, but remain practically undetectable in the X-ray and optical bands unless the effective energy conversion efficiency is sufficiently high.

4.3. Associated thermal emission

As a jet propagating through the AGN accretion disk, a substantial fraction of its energy is deposited into the cocoon (e.g., Bromberg et al. 2011). The subsequent cocoon breakout and adiabatic cooling expansion drive thermal radiation (Tagawa et al. 2024; Rodríguez-Ramírez et al. 2024; Chen & Dai 2025), accompanying the nonthermal emission produced by the jet.

For powerful uncollimated jets, such as successful GRB jets, the thermal flare in the soft X-ray band is substantially weaker than its nonthermal counterpart in both duration ($< O(10^3)$ s) and luminosity ($< O(10^{47})$ erg s⁻¹), as shown in Figure 9 of Chen & Dai (2025); consequently, its contribution to the total observed flux is negligible. The optical thermal flare emerges at $> O(10^4)$ s, by which time the nonthermal flare has faded significantly, whereas the thermal component persists for a longer duration $> O(10^5)$ s, contributing to the observed optical radiation. For long-lived free jets, e.g., BBH merger remnant-driven jets, the optical thermal flare is dimmer than the AGN background and therefore undetectable. In contrast, the cooling cocoon produces a bright transient flare in the soft X-ray band, where the jet nonthermal emission is intrinsically weak; this thermal cocoon component thus serves as a soft X-ray counterpart to the BBH merger event. For jets choked within the AGN disk, cocoon emission constitutes the sole EM signature associated with the jet-launching events.

5. SUMMARY AND DISCUSSION

In this study, motivated by the possibility that relativistic jets embedded in an AGN accretion disk can successfully break out, we have investigated their dynamical evolution and nonthermal emission properties as they propagate through the AGN environment composed of disk-driven winds. By analyzing three representative jet systems—namely, a powerful uncollimated jet, a long-lived free jet, and an under-accelerated jet at breakout—we found that the jet power and dura-

tion jointly govern its global evolution, while the high-density AGN gas gives rise to two characteristic features: rapid dynamical deceleration of the jet ejecta, which induces a prompt downshift in the SED, and persistent strong synchrotron self-absorption, resulting in a distinct quasi-thermal hump in the emission spectrum. Successful relativistic jets can produce observable EM radiations that substantially outshine the AGN background. For BNS/NS-BH mergers or massive stellar core collapse, the resulting GRB jets produce soft X-ray and optical flares lasting several to tens of days, together with infrared and radio transients persisting for months to years. For BBH mergers, jets driven by accretion onto the remnant similarly generate long-lived infrared and radio transients; detectability in the X-ray and optical bands, however, depends strongly on the jet power, making the identification of jet-launching mechanism in BBH mergers crucial for predicting their multi-wavelength signatures. Therefore, binary compact object mergers capable of launching successful relativistic jets are detectable. A key advantage is that rapid dissipation of the jet kinetic energy leads to prompt multiband emission, thereby shortening the time delay between the GW trigger and its EM counterpart, which greatly facilitates a secure association.

Although our analysis focuses on specific illustrative jet systems, the dynamical evolution and the resulting multiband emission of any successfully breaking-out jet can be robustly predicted using the physical framework developed in this study. Combined with our previous work Chen & Dai (2025), which characterizes the thermal emission from jets breaking out of the AGN disk and from the subsequent cocoon cooling expansion, we present a comprehensive framework for predicting the EM signatures of jets launched in AGN disks—regardless of whether they are eventually choked or successfully emerge.

For the AGN environment, we have adopted a simplified, globally uniform wind model. However, AGN outflows exhibit rich structural complexity, spanning a wide range of column densities, velocities, and ionization states across distance scales; even at a fixed radius, outflow properties vary substantially among individual AGNs (Laha et al. 2021). First, AGN winds are not continuous or global, but rather sporadic and spatially fragmented, with different outflow types coexisting in distinct yet overlapping regions. Consequently, the ambient gas density distribution along the jet propagation axis is inherently inhomogeneous and multi-phase. Since variations in ambient density strongly modulate jet dynamics and the resulting emission evolution, the associated multiband light curves may display complex and

anomalous variability patterns. Second, although typical outflow velocities are lower than those of the propagating jet, extreme cases reach up to $0.2c$, comparable to or even exceeding the velocity of jet ejecta during the deep Newtonian phase. Such high-velocity outflows can substantially alter jet dynamics and the corresponding radiative signatures. Third, because the ambient gas is only partially ionized, photoionization induced by the jet radiation field would raise time- and frequency-dependent opacity, leading to distinctive spectral evolution (Ray et al. 2023). In summary, this study outlines the general characteristics of jet evolution and associated its radiation under idealized environmental assumptions. To interpret specific observed events, detailed modeling of multiband light curves will require a tailored construction of the host AGN environment.

Additionally, we have assumed a uniform top-hat jet structure and an on-axis observer geometry. In reality, however, jet material undergoing breakout naturally develops an angular distribution in quantities such as LF and energy density, indicating that successful AGN-disk breakout jets are intrinsically structured (e.g., Got-

lieb et al. 2021). Since both the jet structure and the observer viewing angle strongly affect the emission detectability and variability properties (e.g., Kathirgamaraju et al. 2024; Pang & Dai 2024), the radiative evolution of off-axis structured jets requires further systematic investigation. Furthermore, while a median AGN SED is adopted to estimate the detectability of jet emission, the dispersion among the AGN SED population is large (e.g., Shang et al. 2011). Therefore, for robust modeling of any specific jet event, the individual SED of the host AGN must be employed as the background radiation field.

6. ACKNOWLEDGMENTS

We would like to thank the referee for valuable comments and Sen-Lin Pang for helpful discussions. This work was supported by the National Natural Science Foundation of China (grant No. 12393812), and the Strategic Priority Research Program of the Chinese Academy of Sciences (grant NO. XDB0550300).

APPENDIX

A. SYNCHROTRON SELF-ABSORPTION FREQUENCY

In the strong self-absorption regime, where $\nu'_a > \nu'_c$, the thermal hump dominates over the initial synchrotron emission around ν'_a , thereby self-consistently setting the absorption frequency (Kobayashi et al. 2004). Under a heating-cooling balance, the total energy of self-absorbed synchrotron radiation E_a is reprocessed and emitted around ν'_a in a dynamical time, and the corresponding specific emission luminosity can be estimated as $L_{\nu'_a} \simeq E_a/\nu'_a t'$.

When the spectral ordering satisfies $\nu'_a > \nu'_m > \nu'_c$, the initial self-absorbed synchrotron photons consume the energy deposited in electrons between γ_m and γ_a following the distribution of Equation (24), i.e., $E_a \sim \frac{p-1}{p-2} \xi_e N_{\text{tot}} \gamma_m m_e c^2 / (1 + Y_{\text{TOT}})$, and thereby

$$L_{\nu'_a} = C \left(\frac{\nu'_m \nu'_c}{\nu'^2_a} \right)^{\frac{1}{2}} \frac{\tilde{\gamma}_c}{\gamma_c} L_{\nu, \text{max}}, \quad (\text{A1})$$

with $C = \frac{16\pi}{27\sqrt{3}} \frac{p-1}{p-2}$, $L_{\nu, \text{max}} = \xi_e N_{\text{tot}} P_{\nu, \text{max}}$, and the factor $\tilde{\gamma}_c/\gamma_c$ arises because only a fraction of the total relativistic electrons contribute to the instantaneous emission on account of the very fast cooling of electron when $\tilde{\gamma}_c \ll 1$ (Beniamini & Piran 2013; Rahaman et al. 2025). This luminosity exceeds the unabsorbed synchrotron contribution at ν'_a , which reads

$$L_{\nu'_a} = C \left(\frac{\nu'_m}{\nu'_a} \right)^{1-\frac{p}{2}} L_{\nu'_a, \text{syn}}, \quad (\text{A2})$$

where (Zhang 2018)

$$L_{\nu'_a, \text{syn}} = \left(\frac{\nu'_c}{\nu'_m} \right)^{\frac{1}{2}} \left(\frac{\nu'_m}{\nu'_a} \right)^{\frac{p}{2}} \frac{\tilde{\gamma}_c}{\gamma_c} L_{\nu, \text{max}}. \quad (\text{A3})$$

Consequently, a distinctive spectral hump appears around ν'_a , above which the spectrum resumes the standard synchrotron power-law form (Ghisellini et al. 1988). When $\nu'_m > \nu'_a > \nu'_c$, the majority of photon energy is successfully radiated around ν'_m , while the self-absorbed energy below ν'_a is reduced by a factor of $(\nu'_a/\nu'_m)^{1/2}$ relative to the $\nu'_a > \nu'_m > \nu'_c$ case, and correspondingly

$$L_{\nu'_a} = C \left(\frac{\nu'_c}{\nu'_a} \right)^{\frac{1}{2}} \frac{\tilde{\gamma}_c}{\gamma_c} L_{\nu, \text{max}} = CL_{\nu'_a, \text{syn}}, \quad (\text{A4})$$

which is slightly larger than the original synchrotron emission. For the case of $\nu'_a > \nu'_c > \nu'_m$, only electrons with LF larger than γ_c cool effectively on a dynamical time. The self-absorption energy now corresponds to the energy deposited in electrons between γ_c and γ_a , i.e., $E_a \sim \frac{p-1}{p-2} (\gamma_c/\gamma_m)^{1-p} \gamma_c N_{\text{tot}} m_e c^2 / (1 + Y_{\text{TOT}})$, and thus

$$L_{\nu'_a} = C \left(\frac{\nu'_c}{\nu'_m} \right)^{\frac{1-p}{2}} \frac{\nu'_c}{\nu'_a} L_{\nu, \text{max}} = C \left(\frac{\nu'_c}{\nu'_a} \right)^{1-\frac{p}{2}} L_{\nu'_a, \text{syn}}, \quad (\text{A5})$$

where (Zhang 2018)

$$L_{\nu'_a, \text{syn}} = \left(\frac{\nu'_c}{\nu'_m} \right)^{-\frac{p-1}{2}} \left(\frac{\nu'_c}{\nu'_a} \right)^{\frac{p}{2}} L_{\nu, \text{max}}. \quad (\text{A6})$$

Employing $I_{\nu'_a} = 2\gamma_a m_e \nu'_a{}^2$ and estimating $I_{\nu'_a} \sim L_{\nu'_a} / 4\pi^2 \theta^2 r^2$, the synchrotron self-absorption frequency is derived as

$$\nu'_a = \left(\frac{C I_{\nu, \text{max}}}{2m_e} \sqrt{\frac{3eB'}{2\pi m_e c}} \right)^{\frac{2}{7}} \begin{cases} (\nu'_m \nu'_c)^{\frac{1}{7}}, & \nu'_c < \nu'_m < \nu'_a \\ \nu'_c{}^{\frac{1}{7}}, & \nu'_c < \nu'_a < \nu'_m \\ \nu'_c{}^{\frac{2}{7}} \left(\frac{\nu'_c}{\nu'_m} \right)^{\frac{1-p}{7}}, & \nu'_m < \nu'_c < \nu'_a \end{cases} \quad (\text{A7})$$

where $I_{\nu, \text{max}} \sim \xi_e (\bar{\gamma}_c / \gamma_c) N_{\text{tot}} P_{\nu, \text{max}} / 4\pi^2 \theta^2 r^2$.

In the weak self-absorption regime where $\nu'_a < \nu'_c$, employing Equation (42), the synchrotron self-absorption frequency is given by (Wang et al. 2026)

$$\nu'_a = \begin{cases} \left(\frac{I_{\nu, \text{max}}}{2\gamma_p m_e \nu_p'^{1/3}} \right)^{\frac{3}{5}}, & \nu'_a < \min[\nu'_m, \nu'_c] \\ \left(\frac{I_{\nu, \text{max}}}{2m_e} \sqrt{\frac{3eB'}{2\pi m_e c}} \right)^{\frac{2}{p+4}} \nu_m'^{\frac{p-1}{p+4}}, & \nu'_m < \nu'_a < \nu'_c \end{cases} \quad (\text{A8})$$

where $\nu_p' = \min[\nu'_m, \nu'_c]$.

B. ELECTRON ENERGY DISTRIBUTIONS AND SYNCHROTRON RADIATION SPECTRA

In the strong absorption regime, where $\nu_a > \nu_c$, synchrotron self-absorption thermalizes the electron population below γ_a , driving both the electron energy distribution and the emitted synchrotron spectrum toward a quasi-thermal form. This results in a thermal bump in the electron distribution near γ_a , accompanied by a corresponding pronounced thermal hump at ν_a . Above γ_a and ν_a , the distributions recover their standard power-law forms (Ghisellini et al. 1988).

For the case $\gamma_a > \gamma_m > \gamma_c$, the heated electrons with LF around γ_a share E_a , the corresponding number density can be estimated as $N_e(\gamma_a) \sim (\gamma_m/\gamma_a) \xi_e N_{\text{tot}}$. Therefore, the modified energy distribution of the instantaneously radiating electrons is

$$\frac{dN_e}{d\gamma} = N_{e, \text{syn}} \begin{cases} 3\gamma_m \gamma_a^{-4} \gamma^2, & \gamma < \gamma_a \\ \gamma_m^{p-1} \gamma_c \gamma^{-p-1}, & \gamma > \gamma_a \end{cases} \quad (\text{B1})$$

where $N_{e, \text{syn}} = \xi_e (\bar{\gamma}_c / \gamma_c) N_{\text{tot}}$. Here, the low- γ branch represents the quasi-thermal excess induced by SSA, while the high- γ branch retains the standard cooled power law. Adopting the peak specific luminosity from Equation (A1), the observed synchrotron spectrum is approximately given by

$$F_{\nu, \text{syn}}(\nu) = F_{\text{syn}, \text{max}} e^{-\frac{\nu}{\nu_a}} \begin{cases} C \left(\frac{\nu_m \nu_c}{\nu_a^2} \right)^{\frac{1}{2}} \left(\frac{\nu}{\nu_a} \right)^2, & \nu < \nu_a \\ \left(\frac{\nu_c}{\nu_m} \right)^{\frac{1}{2}} \left(\frac{\nu_m}{\nu_a} \right)^{\frac{p}{2}} \left(\frac{\nu}{\nu_a} \right)^{-\frac{p}{2}}, & \nu > \nu_a \end{cases} \quad (\text{B2})$$

with an exponential cutoff at high energies, where $F_{\text{syn}, \text{max}} = \Gamma N_{e, \text{syn}} P_{\nu, \text{max}} / 4\pi D_L^2$ for an on-axis observer, and D_L is the luminosity distance of the emission source. In reality, the actual spectral transition across the thermal hump near ν_a is smoothed rather than a sharp cutoff; nevertheless, the piecewise power-law approximation given by Equation

(B2) robustly captures the dominant spectral shape (Gao et al. 2013a). To ensure spectral continuity, we model the emission above ν_a using a simplified quasi-thermal spectrum (Kobayashi et al. 2004), where the flux declines beyond the peak as $\exp(1 - \nu/\nu_a)$, until connecting to the non-thermal part of the spectrum.

For the case $\gamma_m > \gamma_a > \gamma_c$, most of the electrons are cooling to γ_a , and the modified energy distribution is

$$\frac{dN_e}{d\gamma} = N_{e,\text{syn}} \begin{cases} 3\gamma_a^{-3}\gamma^2, & \gamma < \gamma_a \\ \gamma_c\gamma^{-2}, & \gamma_a < \gamma < \gamma_m \\ \gamma_m^{p-1}\gamma_c\gamma^{-p-1}. & \gamma > \gamma_m \end{cases} \quad (\text{B3})$$

The synchrotron spectrum is approximately given by

$$F_{\nu,\text{syn}}(\nu) = F_{\text{syn,max}} e^{-\frac{\nu}{\nu_M}} \begin{cases} C \left(\frac{\nu_c}{\nu_a}\right)^{\frac{1}{2}} \left(\frac{\nu}{\nu_a}\right)^2, & \nu < \nu_a \\ \left(\frac{\nu_c}{\nu_a}\right)^{\frac{1}{2}} \left(\frac{\nu}{\nu_a}\right)^{-\frac{1}{2}}, & \nu_a < \nu < \nu_m \\ \left(\frac{\nu_c}{\nu_m}\right)^{\frac{1}{2}} \left(\frac{\nu}{\nu_m}\right)^{-\frac{p}{2}}. & \nu > \nu_m \end{cases} \quad (\text{B4})$$

For the case $\gamma_a > \gamma_c > \gamma_m$, the electron number density around γ_a can be estimated as $N_{e,\text{SSA}} \sim E_a/\gamma_a m_e c^2$, and

$$\frac{dN_e}{d\gamma} = N_{e,\text{syn}} \begin{cases} 3\gamma_m^{p-1}\gamma_c^{2-p}\gamma_a^{-4}\gamma^2, & \gamma < \gamma_a \\ (p-1)\gamma_m^{p-1}\gamma_c\gamma^{-p-1}. & \gamma > \gamma_a \end{cases} \quad (\text{B5})$$

Adopting the peak specific luminosity of Equation (A5), the synchrotron spectrum is thus given by

$$F_{\nu,\text{syn}}(\nu) = F_{\text{syn,max}} e^{-\frac{\nu}{\nu_M}} \begin{cases} C \left(\frac{\nu_c}{\nu_a}\right) \left(\frac{\nu_c}{\nu_m}\right)^{\frac{1-p}{2}} \left(\frac{\nu}{\nu_a}\right)^2, & \nu < \nu_a \\ \left(\frac{\nu_c}{\nu_m}\right)^{\frac{1-p}{2}} \left(\frac{\nu_c}{\nu_a}\right)^{\frac{p}{2}} \left(\frac{\nu}{\nu_a}\right)^{-\frac{p}{2}}. & \nu > \nu_a \end{cases} \quad (\text{B6})$$

In the weak self-absorption regime, where $\nu_a < \nu_c$, the electron energy distribution and the corresponding synchrotron spectrum have been extensively studied and are now well established within the standard afterglow model (Sari et al. 1998; Granot & Sari 2002; Gao et al. 2013b; Wang et al. 2026). We therefore adopt this standard framework without further elaboration.

REFERENCES

- Abac, A. G., Abouelfettouh, I., Acernese, F., et al. 2025, ApJL, 993, 1, L25. doi:10.3847/2041-8213/ae0c9c
- Abbott, B. P., Abbott, R., Abbott, T. D., et al. 2017a, PhRvL, 119, 16, 161101. doi:10.1103/PhysRevLett.119.161101
- Abbott, B. P., Abbott, R., Abbott, T. D., et al. 2017b, ApJL, 848, 2, L12. doi:10.3847/2041-8213/aa91c9
- Abbott, R., Abbott, T. D., Abraham, S., et al. 2020, PhRvL, 125, 10, 101102. doi:10.1103/PhysRevLett.125.101102
- Bartos, I. & Haiman, Z. 2026, ApJL, 996, 2, L44. doi:10.3847/2041-8213/ae2bff
- Begelman, M. C. & Cioffi, D. F. 1989, ApJL, 345, L21. doi:10.1086/185542
- Bellm, E. 2014, The Third Hot-wiring the Transient Universe Workshop, 27. doi:10.48550/arXiv.1410.8185
- Beniamini, P. & Piran, T. 2013, ApJ, 769, 1, 69. doi:10.1088/0004-637X/769/1/69
- Bromberg, O., Nakar, E., Piran, T., et al. 2011, ApJ, 740, 2, 100. doi:10.1088/0004-637X/740/2/100
- Chen, K. & Dai, Z.-G. 2025, ApJ, 987, 2, 214. doi:10.3847/1538-4357/addb48
- Chen, K. & Dai, Z.-G. 2024, ApJ, 961, 2, 206. doi:10.3847/1538-4357/ad0dfd

- Chen, K., Ren, J., & Dai, Z.-G. 2023, *ApJ*, 948, 2, 136. doi:10.3847/1538-4357/acc45f
- Delfavero, V., Ford, K. E. S., McKernan, B., et al. 2025, *ApJ*, 989, 1, 67. doi:10.3847/1538-4357/ade4c1
- Dittmann, A. J., Cantiello, M., & Jermyn, A. S. 2021, *ApJ*, 916, 1, 48. doi:10.3847/1538-4357/ac042c
- Fabj, G., Dittmann, A. J., Cantiello, M., et al. 2025, *ApJ*, 981, 1, 16. doi:10.3847/1538-4357/ada896
- Ford, K. E. S. & McKernan, B. 2025, , arXiv:2506.08801. doi:10.48550/arXiv.2506.08801
- Gao, H., Lei, W.-H., Wu, X.-F., et al. 2013, *MNRAS*, 435, 3, 2520. doi:10.1093/mnras/stt1461
- Gao, H., Lei, W.-H., Zou, Y.-C., et al. 2013, *NewAR*, 57, 6, 141. doi:10.1016/j.newar.2013.10.001
- Ghisellini, G., Guilbert, P. W., & Svensson, R. 1988, *ApJL*, 334, L5. doi:10.1086/185300
- Giustini, M. & Proga, D. 2019, *A&A*, 630, A94. doi:10.1051/0004-6361/201833810
- Gottlieb, O., Nakar, E., & Bromberg, O. 2021, *MNRAS*, 500, 3, 3511. doi:10.1093/mnras/staa3501
- Graham, M. J., Ford, K. E. S., McKernan, B., et al. 2020, *PhRvL*, 124, 25, 251102. doi:10.1103/PhysRevLett.124.251102
- Granot, J., Ramirez-Ruiz, E., Taylor, G. B., et al. 2006, *ApJ*, 638, 1, 391. doi:10.1086/497680
- Granot, J. & Sari, R. 2002, *ApJ*, 568, 2, 820. doi:10.1086/338966
- He, L., Zhu, L.-G., Liu, Z.-Y., et al. 2025, , arXiv:2511.05144. doi:10.48550/arXiv.2511.05144
- Huang, B.-Q., Liu, T., Li, X.-Y., et al. 2024, *ApJ*, 967, 1, 67. doi:10.3847/1538-4357/ad3d54
- Huang, Y. F. & Cheng, K. S. 2003, *MNRAS*, 341, 1, 263. doi:10.1046/j.1365-8711.2003.06430.x
- Huang, Y. F., Gou, L. J., Dai, Z. G., et al. 2000, *ApJ*, 543, 1, 90. doi:10.1086/317076
- Ishibashi, W. & Gröbner, M. 2024, *MNRAS*, 529, 2, 883. doi:10.1093/mnras/stae569
- Jermyn, A. S., Dittmann, A. J., Cantiello, M., et al. 2021, *ApJ*, 914, 2, 105. doi:10.3847/1538-4357/abfb67
- Kaaz, N., Murguia-Berthier, A., Chatterjee, K., et al. 2023, *ApJ*, 950, 1, 31. doi:10.3847/1538-4357/acc7a1
- Kang, H. D., Perna, R., Lazzati, D., et al. 2025, *The Open Journal of Astrophysics*, 8, 23. doi:10.33232/001c.131902
- Kathirgamaraju, A., Li, H., Ryan, B. R., et al. 2024, *ApJ*, 972, 1, 101. doi:10.3847/1538-4357/ad63a3
- Kato, S., Fukue, J., & Mineshige, S. 2008, .
- Kim, Y. & Most, E. R. 2025, *PhRvD*, 111, 8, 083025. doi:10.1103/PhysRevD.111.083025
- King, A. & Pounds, K. 2015, *ARA&A*, 53, 115. doi:10.1146/annurev-astro-082214-122316
- Kobayashi, S., Mészáros, P., & Zhang, B. 2004, *ApJL*, 601, 1, L13. doi:10.1086/381733
- Kobayashi, S. & Zhang, B. 2003, *ApJL*, 582, 2, L75. doi:10.1086/367691
- Laha, S., Reynolds, C. S., Reeves, J., et al. 2021, *Nature Astronomy*, 5, 13. doi:10.1038/s41550-020-01255-2
- Lazzati, D., Soares, G., & Perna, R. 2022, *ApJL*, 938, 2, L18. doi:10.3847/2041-8213/ac98ad
- Lei, L., Zhu, Q.-F., Kong, X., et al. 2023, *Research in Astronomy and Astrophysics*, 23, 3, 035013. doi:10.1088/1674-4527/acb877
- Lyu, J. & Rieke, G. H. 2017, *ApJ*, 841, 2, 76. doi:10.3847/1538-4357/aa7051
- Matzner, C. D. 2003, *MNRAS*, 345, 2, 575. doi:10.1046/j.1365-8711.2003.06969.x
- McKernan, B., Ford, K. E. S., Cook, H. E., et al. 2025, *ApJ*, 990, 2, 217. doi:10.3847/1538-4357/adf114
- McKernan, B., Ford, K. E. S., & O’Shaughnessy, R. 2020, *MNRAS*, 498, 3, 4088. doi:10.1093/mnras/staa2681
- Metzger, B. D., Giannios, D., & Mimica, P. 2012, *MNRAS*, 420, 4, 3528. doi:10.1111/j.1365-2966.2011.20273.x
- McPike, E., Perna, R., Ford, K. E. S., et al. 2026, arXiv:2602.04135. doi:10.48550/arXiv.2602.04135
- Mizuta, A. & Ioka, K. 2013, *ApJ*, 777, 2, 162. doi:10.1088/0004-637X/777/2/162
- Nakar, E. & Piran, T. 2017, *ApJ*, 834, 1, 28. doi:10.3847/1538-4357/834/1/28
- Nakar, E. & Sari, R. 2012, *ApJ*, 747, 2, 88. doi:10.1088/0004-637X/747/2/88
- Nakar, E., Piran, T., & Sari, R. 2005, *ApJ*, 635, 1, 516. doi:10.1086/497296
- Netzer, H. 2013, .
- Pang, S.-L. & Dai, Z.-G. 2024, *ApJ*, 977, 1, 123. doi:10.3847/1538-4357/ad9007
- Perna, R., Tagawa, H., Haiman, Z., et al. 2021z, *ApJ*, 915, 1, 10. doi:10.3847/1538-4357/abfdb4
- Perna, R., Lazzati, D., & Cantiello, M. 2021b, *ApJL*, 906, 2, L7. doi:10.3847/2041-8213/abd319
- Proga, D., Stone, J. M., & Kallman, T. R. 2000, *ApJ*, 543, 2, 686. doi:10.1086/317154
- Rahaman, S. M., Granot, J., & Beniamini, P. 2025, *ApJL*, 988, 2, L68. doi:10.3847/2041-8213/aded07
- Ray, M., Lazzati, D., & Perna, R. 2023, *MNRAS*, 521, 3, 4233. doi:10.1093/mnras/stad816
- Risaliti, G. & Elvis, M. 2010, *A&A*, 516, A89. doi:10.1051/0004-6361/200912579
- Rodríguez-Ramírez, J. C., Bom, C. R., Fraga, B., et al. 2024, *MNRAS*, 527, 3, 6076. doi:10.1093/mnras/stad3575

- Rossi, E. M., Lodato, G., Armitage, P. J., et al. 2010, *MNRAS*, 401, 3, 2021. doi:10.1111/j.1365-2966.2009.15802.x
- Rowan, C., Whitehead, H., & Kocsis, B. 2025, *MNRAS*, 544, 4, 4576. doi:10.1093/mnras/staf1896
- Rybicki, G. B. & Lightman, A. P. 1979, .
- Santana, R., Barniol Duran, R., & Kumar, P. 2014, *ApJ*, 785, 1, 29. doi:10.1088/0004-637X/785/1/29
- Sari, R. & Esin, A. A. 2001, *ApJ*, 548, 2, 787. doi:10.1086/319003
- Sari, R. & Piran, T. 1999, *ApJ*, 520, 2, 641. doi:10.1086/307508
- Sari, R., Piran, T., & Narayan, R. 1998, *ApJL*, 497, 1, L17. doi:10.1086/311269
- Sari, R. & Piran, T. 1995, *ApJL*, 455, L143. doi:10.1086/309835
- Salvesen, G., Simon, J. B., Armitage, P. J., et al. 2016, *MNRAS*, 457, 1, 857. doi:10.1093/mnras/stw029
- Shang, Z., Brotherton, M. S., Wills, B. J., et al. 2011, *ApJS*, 196, 1, 2. doi:10.1088/0067-0049/196/1/2
- Shen, R.-F. & Zhang, B. 2009, *MNRAS*, 398, 4, 1936. doi:10.1111/j.1365-2966.2009.15212.x
- Sirko, E. & Goodman, J. 2003, *MNRAS*, 341, 2, 501. doi:10.1046/j.1365-8711.2003.06431.x
- Sironi, L., Spitkovsky, A., & Arons, J. 2013, *ApJ*, 771, 1, 54. doi:10.1088/0004-637X/771/1/54
- Symeonidis, M., GIBLIN, B. M., Page, M. J., et al. 2016, *MNRAS*, 459, 1, 257. doi:10.1093/mnras/stw667
- Tagawa, H., Haiman, Z., Kimura, S. S., et al. 2026, arXiv:2604.05020. doi:10.48550/arXiv.2604.05020
- Tagawa, H., Kimura, S. S., Haiman, Z., et al. 2024, *ApJ*, 966, 1, 21. doi:10.3847/1538-4357/ad2e0b
- Tagawa, H., Kimura, S. S., Haiman, Z., et al. 2023, *ApJ*, 950, 1, 13. doi:10.3847/1538-4357/acc4bb
- Tagawa, H., Haiman, Z., & Kocsis, B. 2020, *ApJ*, 898, 1, 25. doi:10.3847/1538-4357/ab9b8c
- Wang, J.-M., Liu, J.-R., Ho, L. C., et al. 2021, *ApJL*, 916, 2, L17. doi:10.3847/2041-8213/ac0b46
- Wang, X.-G., Zhang, B., Liang, E.-W., et al. 2015, *ApJS*, 219, 1, 9. doi:10.1088/0067-0049/219/1/9
- Wang, Y., Chen, C., & Zhang, B. 2026, *Journal of High Energy Astrophysics*, 50, 100490. doi:10.1016/j.jheap.2025.100490
- Wang, Y.-H., Lazzati, D., & Perna, R. 2022, *MNRAS*, 516, 4, 5935. doi:10.1093/mnras/stac1968
- Wei, Y.-F., Liu, T., & Huang, B.-Q. 2025, *ApJ*, 995, 1, 121. doi:10.3847/1538-4357/ae2256
- Woosley, S. E. & Bloom, J. S. 2006a, *ARA&A*, 44, 1, 507. doi:10.1146/annurev.astro.43.072103.150558
- Woosley, S. E. & Heger, A. 2006b, *ApJ*, 637, 2, 914. doi:10.1086/498500
- Woosley, S. E. 1993, *ApJ*, 405, 273. doi:10.1086/172359
- Yang, Y., Gayathri, V., Bartos, I., et al. 2020, *ApJL*, 901, 2, L34. doi:10.3847/2041-8213/abb940
- Yi, S.-X., Wu, X.-F., & Dai, Z.-G. 2013, *ApJ*, 776, 2, 120. doi:10.1088/0004-637X/776/2/120
- Yuan, H.-Y. & Lei, W.-H. 2025, *ApJ*, 987, 2, 167. doi:10.3847/1538-4357/addbe4
- Yuan, W., Zhang, C., Chen, Y., et al. 2022, *Handbook of X-ray and Gamma-ray Astrophysics*, 86. doi:10.1007/978-981-16-4544-0_151-1
- Zhang, B. 2018, . doi:10.1017/9781139226530
- Zhang, H.-H., Zhu, J.-P., & Yu, Y.-W. 2024, *ApJ*, 976, 1, 63. doi:10.3847/1538-4357/ad8139
- Zhao, X.-H. 2026, *ApJ*, 997, 1, 112. doi:10.3847/1538-4357/ae21c1
- Zhou, Z.-H., Zhu, J.-P., & Wang, K. 2023, *ApJ*, 951, 1, 74. doi:10.3847/1538-4357/acd380
- Zhu, J.-P., Zhang, B., Yu, Y.-W., et al. 2021, *ApJL*, 906, 2, L11. doi:10.3847/2041-8213/abd412
- Zhu, L.-G., He, L., Chen, X., et al. 2026, , arXiv:2601.08286. doi:10.48550/arXiv.2601.08286
- Zhuang, J., Shen, R.-F., Mou, G., et al. 2025, *ApJ*, 979, 2, 109. doi:10.3847/1538-4357/ad9b98